SANDIA REPORT

SAND2015-7909
Unlimited Release
Printed September 2015

Wound Ballistics Modeling for Blast Loading, Blunt Force Impact, and Projectile Penetration

Paul A. Taylor, Candice F. Cooper, and Damon J. Burnett

Prepared by
Sandia National Laboratories
Albuquerque, New Mexico 87185 and Livermore, California 94550

Sandia National Laboratories is a multi-program laboratory managed and operated by Sandia Corporation, a wholly owned subsidiary of Lockheed Martin Corporation, for the U.S. Department of Energy's National Nuclear Security Administration under contract DE-AC04-94AL85000.

Issued by Sandia National Laboratories, operated for the United States Department of Energy by Sandia Corporation.

Available to DOE and DOE contractors from
U.S. Department of Energy
Office of Scientific and Technical Information
P.O. Box 62
Oak Ridge, TN 37831

Telephone: (865) 576-8401
Facsimile: (865) 576-5728
E-Mail: reports@osti.gov
Online ordering: http://www.osti.gov/scitech

Available to the public from
U.S. Department of Commerce
National Technical Information Service
5301 Shawnee Rd
Alexandria, VA 22312

Telephone: (800) 553-6847
Facsimile: (703) 605-6900
E-Mail: orders@ntis.gov
Online order: http://www.ntis.gov/search

SAND2015-7909
Unlimited Release
Printed September 2015

Wound Ballistics Modeling for Blast Loading, Blunt Force Impact, and Projectile Penetration

Paul A. Taylor, Candice F. Cooper, and Damon J. Burnett
Terminal Ballistics Technology
Sandia National Laboratories
P.O. Box 5800
Albuquerque, New Mexico 87185-MS1160

Abstract

Light body armor development for the warfighter is based on trial-and-error testing of prototype designs against ballistic projectiles. Torso armor testing against blast is virtually nonexistent but necessary to ensure adequate protection against injury to the heart and lungs. In this report, we discuss the development of a high-fidelity human torso model, it's merging with the existing Sandia Human Head-Neck Model, and development of the modeling & simulation (M&S) capabilities necessary to simulate wound injury scenarios. Using the new Sandia Human Torso Model, we demonstrate the advantage of virtual simulation in the investigation of wound injury as it relates to the warfighter experience. We present the results of virtual simulations of blast loading and ballistic projectile impact to the torso with and without notional protective armor. In this manner, we demonstrate the advantages of applying a modeling and simulation approach to the investigation of wound injury and relative merit assessments of protective body armor without the need for trial-and-error testing.

ACKNOWLEDGMENTS

We gratefully acknowledge support of the DS&A Precision Engagement LDRD committee and would specifically like to thank Dr. K. Terry Stalker and Dr. David R. Gardner for their valuable feedback and support throughout the lifetime of this project.

CONTENTS

FIGURES

TABLES

NOMENCLATURE

CTH	Sandia Shock Wave Physics Simulation Computer Code (not an acronym)
CSF	Cerebrospinal Fluid
H-N-T	Head-Neck-Torso (model)
M&S	Modeling and Simulation
IED	Improvised Explosive Device
PPE	Personal Protective Equipment
SHT	Sandia Human Torso
TBI	Traumatic Brain Injury
SNL	Sandia National Laboratories

1. INTRODUCTION

To assess personal protective armor performance against ballistic projectiles, the personal armor is placed over ballistic clay and the projectiles are fired into the armor/clay target. The clay is meant to be representative of the human torso and the behind-armor deflection, represented by the depth of the residual impression left in the clay, is the principal metric used to assess armor performance. Although this approach provides a coarse relative merit assessment of protection, it does not speak to the behind-armor blunt trauma suffered by crucial torso organs of the torso. To address this shortcoming, researchers have developed physical torso surrogates possessing embedded pressure sensors, accelerometers, and strain gages measuring thoracic pressures, accelerations, and strains [1,2]. Physical surrogates have the potential to enhance our understanding of the wave mechanics that occur within the thoracic cavity but are constrained to monitoring pressure, acceleration, and strain data at a limited number of locations in the torso. To supplement this effort, we have developed a modeling and simulation (M&S) capability to investigate wound injury scenarios to the head, neck, and torso of a U.S. warfighter.

In this report, we describe the work products of a three year Laboratory Directed Research and Development (LDRD) project to build models representing a human male from the waist up and the simulation methodology with which to conduct virtual wound injury simulations. We demonstrate the use of this toolset to investigate the consequences of, and mitigation against, blast exposure, blunt force impact, and ballistic projectile penetration that lead to damage of critical organs comprising the cardiovascular, respiratory, and central nervous systems. The single most significant deliverable of this project is the newly-developed Sandia Human Torso (SHT) model. This model, when imported into one of our Sandia wave physics computer codes such as CTH, offers an analyst the ability to investigate the details of torso wound injury at a spatial resolution that is unprecedented. Furthermore, the SHT model can be used as a virtual surrogate with which to conduct assessment and optimization of personal armor designs.

Our modeling and simulation (M&S) approach will be shown to have a significant advantage over methods employed by personal armor designers by providing a simulation capability to investigate wound injury mechanics and to optimize armor design without the need for extensive field testing. Furthermore, this approach can be conducted ad infinitum without the use of human cadavers, animal testing, or expensive physical surrogates. Virtual wound injury simulation results can be post-processed to provide stress, strain, energy, stress power, acceleration, and damage measures at as many sites within the virtual model as desired; quantities that are not easily measured, especially at a large number of sites within physical surrogates when exposed to blast or blunt impact.

The remainder of this report is organized as follows. Section 2 contains descriptions of the geometric models developed to represent the torso and the head-neck-torso combination. Section 2 also contains descriptions of the hyperelastic-damage model representations developed for various body components. Section 3 outlines the simulation methods we have employed to investigate various wound injury scenarios. Section 4 presents the simulation results of two types of combat threat scenarios: blast exposure and ballistic projectile impact leading to behind-armor blunt trauma. Concluding remarks about the project work are presented in Section 5 as well as a discussion of future directions for subsequent efforts.

[Blank page following Section]

2. MODELS

2.1 Geometric Models

2.1.1 Human Torso Model

The torso model is based on the National Library of Medicine's Visible Human male data set [3]. The model is constructed by segmenting 495 one millimeter thick axially sliced cryosections of the Visible Human Male into the soft tissue, organs, and bone comprising the torso. The model begins at the base of the neck and continues to just superior to the pelvic region. Specifically, anatomically correct representations of 19 distinct materials including bone, cartilage, intervertebral discs, vasculature/blood, airways/air, lungs, liver, kidneys, spleen, heart, muscle, larynx, stomach, stomach contents, spinal cord, cerebrospinal fluid (CSF), thyroid, abdominal cavity contents, and skin/fat were created by segmenting the various tissues from the 495 axial slices. Our segmentation process maintained high anatomical fidelity, with a spatial resolution of 1 mm (Figure 1). The torso model can be represented in both finite volume and finite element forms, consisting of roughly 42 million elements, for use with Eulerian, Lagrangian, or coupled Lagrangian-Eulerian codes.

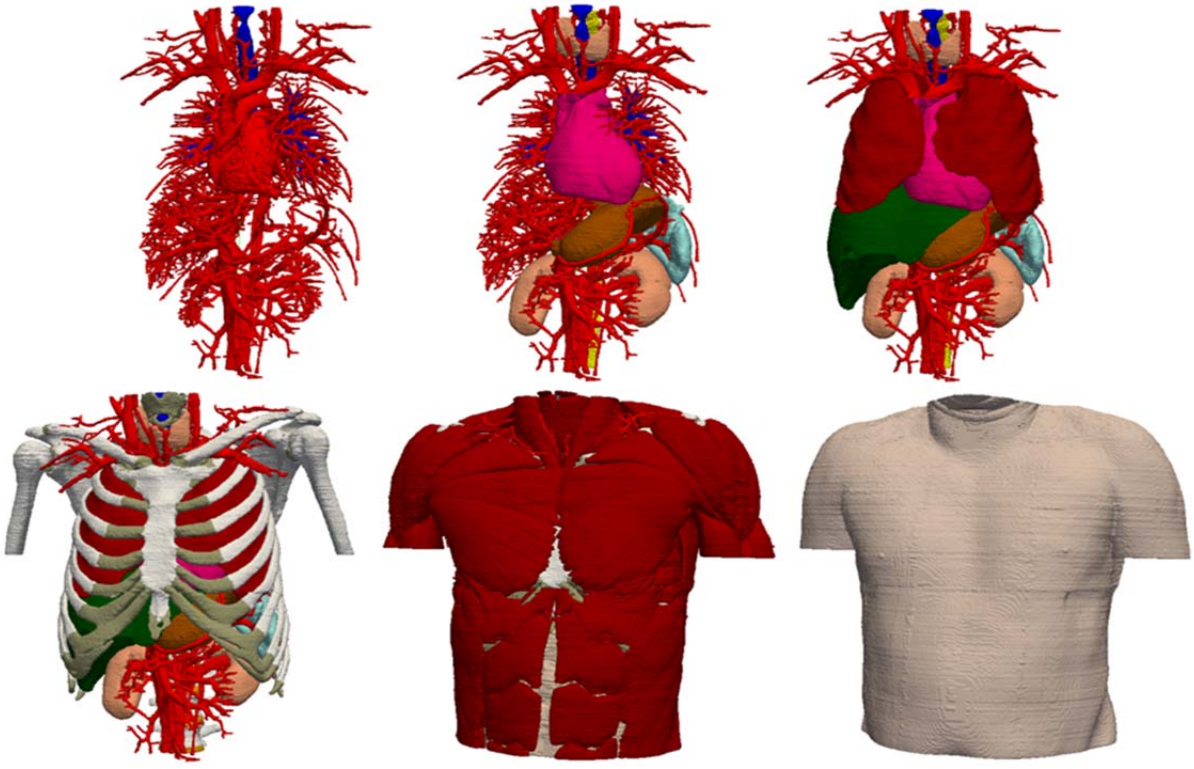

Figure 1. Evolution of Torso Model. Top Left: blood vasculature and airways. Top Center: addition of heart, thyroid, spinal cord, CSF, spleen, kidneys, and stomach. Top Right: addition of lungs and liver. Bottom Left: addition of bone, cartilage, larynx, and intervertebral discs. Bottom Center: addition of muscle and abdominal cavity contents. Bottom Right: addition of fat/skin.

The finite volume version of the torso model, as it has been imported into the Sandia shock physics wave code CTH [4], is displayed in Figure 1. To create the finite element version, the bytemap files, created when the constituent materials are segmented from Visible Human dataset (i.e., organs, tissues, bone, etc.), must undergo a conversion to a finite element format. Local software has been developed specifically for this purpose. The finite element version of the model has not been used extensively since there was no need to employ Lagrangian finite element computational mechanics codes during the execution of this project. That said, if the need arises, conversion software has been developed to create the finite element version of the torso model for use in Lagrangian, finite element analysis.

The torso model is a continuation of the previously completed Sandia head-neck model [5], shown in Figure 2. Both the Sandia head-neck model and Sandia torso model were created from the same Visible Human male data set [3] with the torso model beginning where the head-neck model terminates. Because of this relation, the head-neck and torso models can be joined to create a complete head-neck-torso model.

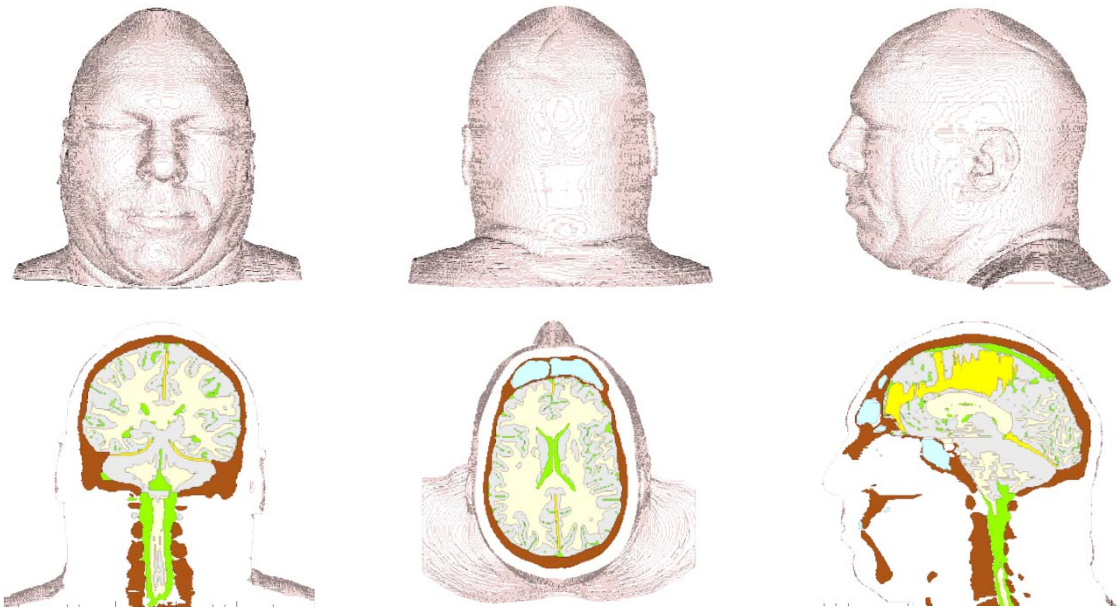

Figure 2. Sandia Head-Neck model; finite volume representation. Model is comprised of bone (skull, mandible, cervical vertebra) white matter, gray matter, falx and tentorium membranes, cerebrospinal fluid, air-filled sinus cavities, and muscle/scalp.

2.1.2 Merged Human Head-Neck-Torso Model

The Sandia Head-Neck-Torso model is a merger of the torso model with the preexisting Sandia Human Head-Neck model. In addition to containing the models representing the constituents of the torso, the merged model also contains the cervical vertebra, skull with mandible, white matter, gray matter, falx/tentorium membranes, cerebrospinal fluid (CSF), and air-filled sinus

cavities. Figure 3 displays the composite head-neck-torso model in both external and sectional views.

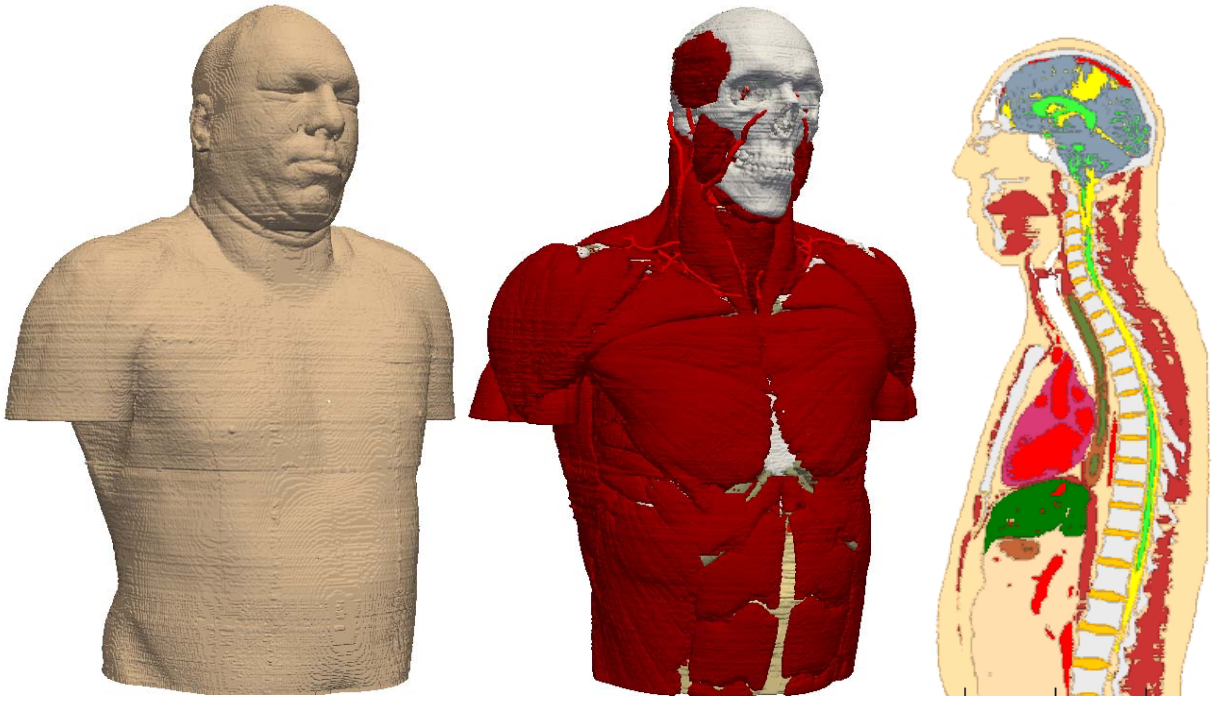

Figure 3. Composite Sandia Head-Neck-Torso model.

2.2 Equation-of-State and Constitutive Model Representations

The dynamic mechanical response of each material comprising the torso is represented by its own distinct equation-of-state and deviatoric constitutive model. These models incorporate the most relevant material properties reported in the scientific literature. An equation-of-state (EOS) describes a material's behavior as it undergoes volumetric changes, which can be either compressive or dilational. In general, an EOS is defined by the following relations:

$$P = \hat{P}(\rho, E) \text{ and } T = \hat{T}(\rho, E), \tag{1}$$

where P is pressure, T is temperature, ρ is mass density, and E is internal energy. To represent the constituent materials of the torso, we have drawn from the existing CTH library of EOS models. In this regard, we have assigned either a Mie-Gruneisen EOS or a Tillotson-Brundage EOS for each material.

The Mie-Gruneisen (M-G) EOS describes the volumetric response of a material experiencing thermomechanical states within some proximity to the material's shock response, as described by its shock Hugoniot curve[1]. The Mie-Gruneisen EOS works well for materials that are not

[1]A shock Hugoniot curve is a material property defined by a loci of shock states that the material can support during shock wave compression, over a range of shock amplitudes.

expected to undergo phase transformations or significant dilational (volume increase) strains. For dilational states, the M-G EOS is linearly extrapolated to the point of failure (fracture), as specified by the simulation code user. For further details on the Mie-Gruneisen EOS and shock Hugoniot, the reader is referred to the report by Hertel and Kerley [6].

The Tillotson-Brundage (T-B) equation-of-state (EOS) [7] is a modified version of the Tillotson EOS [8], originally designed to capture vaporization from compression release for hypervelocity impacts of metals. Brundage [7] has modified the Tillotson EOS by (1) filling in the thermodynamic gaps in ρ-E state space, (2) adding new tensile regions, (3) and adding a fluid cavitation model. Brundage fit the modified Tillotson EOS, referred to here as the Tillotson-Brundage EOS, to represent the response of cerebrospinal fluid based on the data reported in references [9–11] and to human blood using the data reported in references [12,13]. The stomach contents are also modeled using a Tillotson-Brundage EOS representation for water.

In order to simulate blast loading to our human models, air must be included in the simulations. Air envelops the models at ambient conditions, occupies the sinuses, the airways into and throughout the lungs, and transmits the blast waves. For this application, we have employed a non-linear, tabular equation-of-state representation for a dry air mix of N_2 (78.09%), O_2 (21.95%), and Ar (0.96%), reference density of 1.218e-3 g/cm^3, specifically designed for shock wave simulations [6]. The compression Adiabat, generated from our tabular EOS representation for air, is displayed in Figure 4.

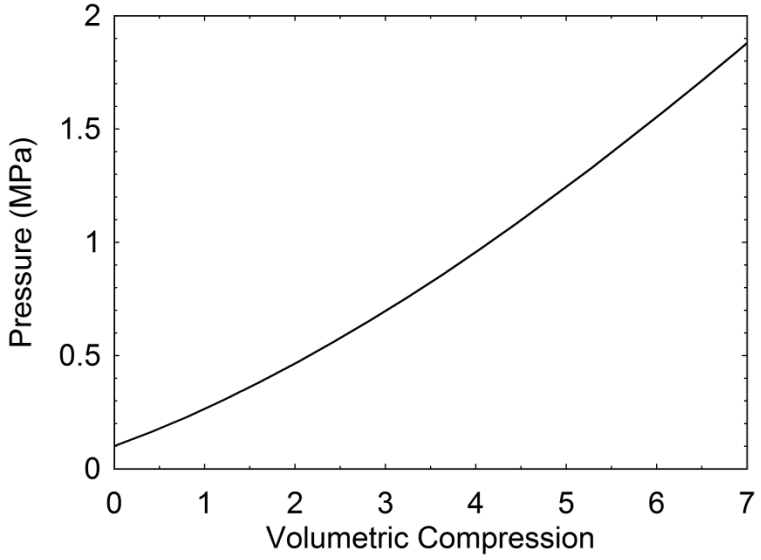

Figure 4. Compression Adiabat describing the volumetric response for dry air; calculated from the tabular EOS representation for this material.

The choice of which EOS is assigned to a particular material depends on whether we expect the material to undergo fluid cavitation. Table 1 displays the assigned EOS and constitutive models representing the volumetric and deviatoric response of each of the materials comprising the torso model.

Our constitutive models have been constructed to describe the deviatoric elastic, viscoelastic, or inelastic response of the material whenever it is subjected to shear or distortional strains. We have employed a number of constitutive models, each representing the 25 respective materials found in human head-neck (6 materials) and torso (19 materials) models.

Early on in the project, we employed simplistic linear elastic, perfectly plastic constitutive models for all materials in order to test our modeling and simulation tools. However, as the project progressed, we developed non-linear hyperelastic constitutive model representations for the materials we considered critical to life support on the battlefield, namely, the lungs, heart, liver, kidneys, and spleen. These model representations are more accurate at capturing the non-linear behavior of the life-critical materials under impulsive loading conditions. Furthermore, the models were complemented by a failure criterion based on exceeding the maximum principal (tensile) strain. For these materials, we implemented a condensed version of the Swanson Hyperelastic model [14]. The specific form for this model starts with the definition of a strain energy potential function:

$$U = \frac{3}{2}\frac{A_1}{P_1+1}\left(\frac{\bar{I}_1}{3}-1\right)^{P_1+1} + \frac{3}{2}\frac{B_1}{Q_1+1}\left(\frac{\bar{I}_2}{3}-1\right)^{Q_1+1} + \frac{3}{2}\frac{C_1}{R_1+1}\left(\frac{\bar{I}_1}{3}-1\right)^{R_1+1}, \tag{2}$$

where $\bar{I}_1$ and $\bar{I}_2$ are the first and second invariants of the volume preserving left Cauchy-Green strain tensor $\bar{\boldsymbol{B}}$, defined in terms of the deformation gradient according to the equations

$$\bar{\boldsymbol{B}} = \bar{\boldsymbol{F}}\bar{\boldsymbol{F}}^T, \quad \bar{\boldsymbol{F}} = J^{-1/3}\boldsymbol{F}, \quad \text{and} \quad J = \det(\boldsymbol{F}). \tag{3}$$

In eq.(3), $\boldsymbol{F}$ is the deformation gradient and J is its determinate, also known as the Jacobian. The invariants $\bar{I}_1$ and $\bar{I}_2$ are defined as

$$\bar{I}_1 = tr(\bar{\boldsymbol{B}}) \quad \text{and} \quad \bar{I}_2 = \frac{1}{2}[\bar{I}_1^{\,2} - tr(\bar{\boldsymbol{B}}\bar{\boldsymbol{B}})], \tag{4}$$

where $tr(*)$ denotes the trace of its tensor argument.

The Cauchy stress is defined as

$$\boldsymbol{\sigma} = \frac{2}{J}\left[\left(\frac{\partial U}{\partial \bar{I}_1} + \bar{I}_1\frac{\partial U}{\partial \bar{I}_2}\right)\bar{\boldsymbol{B}} - \frac{\partial U}{\partial \bar{I}_2}\bar{\boldsymbol{B}}\bar{\boldsymbol{B}}\right], \tag{5}$$

with J, U, $\bar{I}_1$ and $\bar{I}_2$, and $\bar{\boldsymbol{B}}$ defined according to eqs.(2)-(4) above. Since we only use the deviatoric form of the Cauchy stress for our constitutive model representation, we employ the following definition of deviatoric (Cauchy) stress $\boldsymbol{S}$:

$$\boldsymbol{S} = \boldsymbol{\sigma} - \frac{1}{3}tr(\boldsymbol{\sigma})\mathbf{1}. \tag{6}$$

Failure is implemented by monitoring the maximum principal strain of the Lagrangian strain tensor $\boldsymbol{E}$, defined as

$$\boldsymbol{E} = \frac{1}{2}(\boldsymbol{F}^T\boldsymbol{F} - \mathbf{1}). \tag{7}$$

If we denote the maximum principal strain of $\boldsymbol{E}$ as e_1, then our model assumes the material has failed and cannot support tensile strains if the principal strain exceeds the critical tensile value, i.e., failure occurs if

$$e_1 \geq e_{critical} \quad \text{for} \quad e_1 > 0. \tag{8}$$

In our simulations, the critical failure strain $e_{critical}$ is considered to be a material property.

Once the failure criterion in eq.(8) is satisfied for a particular material within a specific computational cell, we diminish the ability of that material to support normal tensile stresses, over a predefined period of time (typically 10 time steps). The progressive reduction of the normal stresses for a failed material is performed so that we do not inadvertently introduce local wave disturbances from the abrupt release of stored strain energy as a consequence of reducing the material's strength from undamaged to fully damaged in a single time step.

The fitting of our version of the Swanson hyperelastic model to lung [15], heart [16], liver [17], kidney[18], spleen [17,19], and muscle [20] tissue data is displayed in Figures 5-9. For these materials, we attempted to fit all available data, including the uniaxial compressive and tensile responses, with emphasis placed on fitting the compressive response data more accurately, if it existed. Specifically, our Swanson model fits of the data for liver, kidney, spleen, and muscle placed emphasis on accurately capturing the compression regime of the materials' response with the tensile regime fit given subordinate priority. This approach is not overly restrictive since we expect these materials to be under compressive and shear loading the majority of the time in our simulations. The two exceptions were the lungs and heart, where only lung tensile data and heart shear data was available. Our fits of these data is shown in Figure 5.

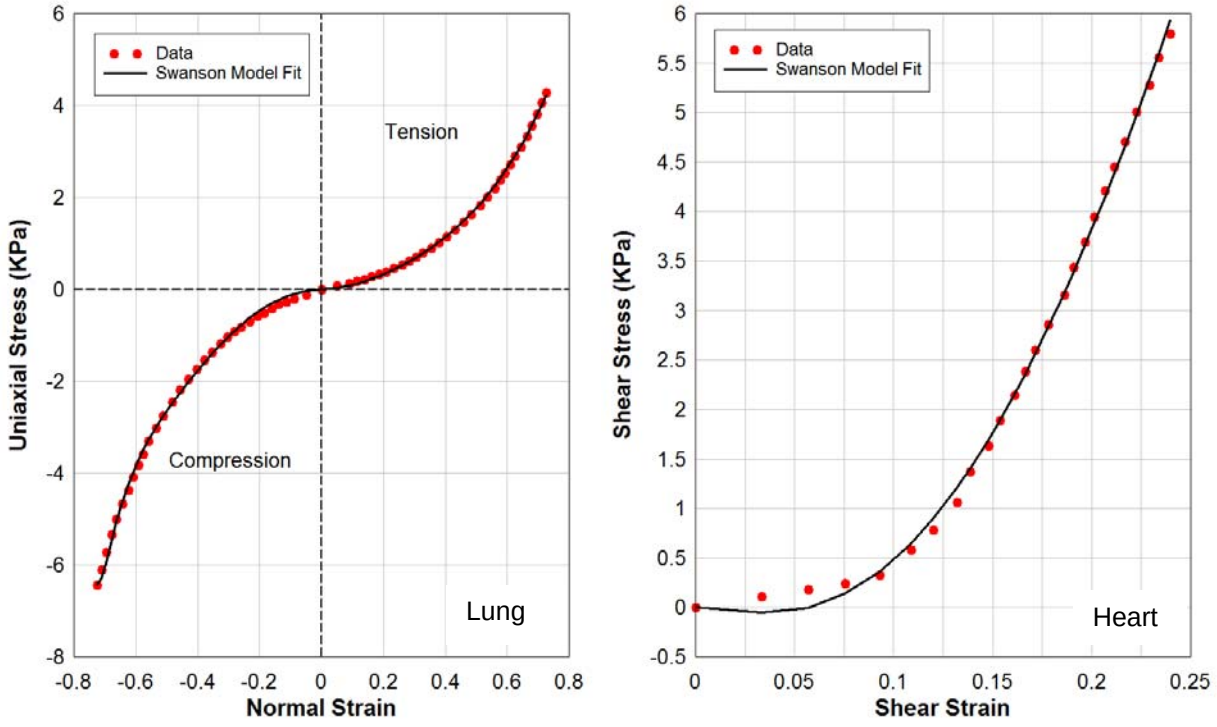

Figure 5. Plots of Swanson model fit with experimental data. Left: Lung, Right: Heart.

The Swanson model parameters associated with the fits to data as depicted in Figures 5-7 are listed in Table 1.

Bone material is represented by a Mie-Gruneisen EOS and a linear elastic, perfectly-plastic deviatoric constitutive model with an accumulated plastic strain-to-failure fracture model. These models are fit to material properties data reported by Zhang et al. [21] and Carter [22] for cortical bone. Specifically, volumetric response of bone is represented by a Mie-Gruneisen EOS, fit to published literature values of mass density and bulk modulus. The material's deviatoric response is fit using published values for shear modulus and fracture strength.

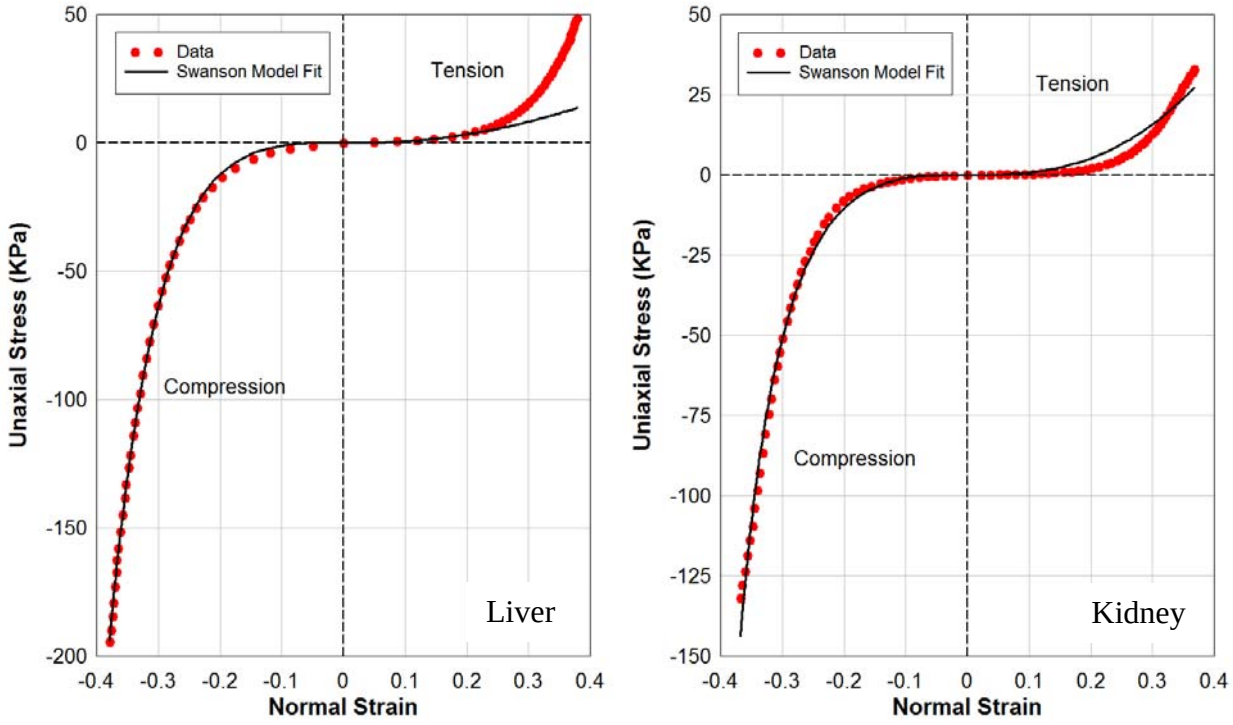

Figure 6. Plots of Swanson model fit with experimental data. Left: Liver, Right: Kidney.

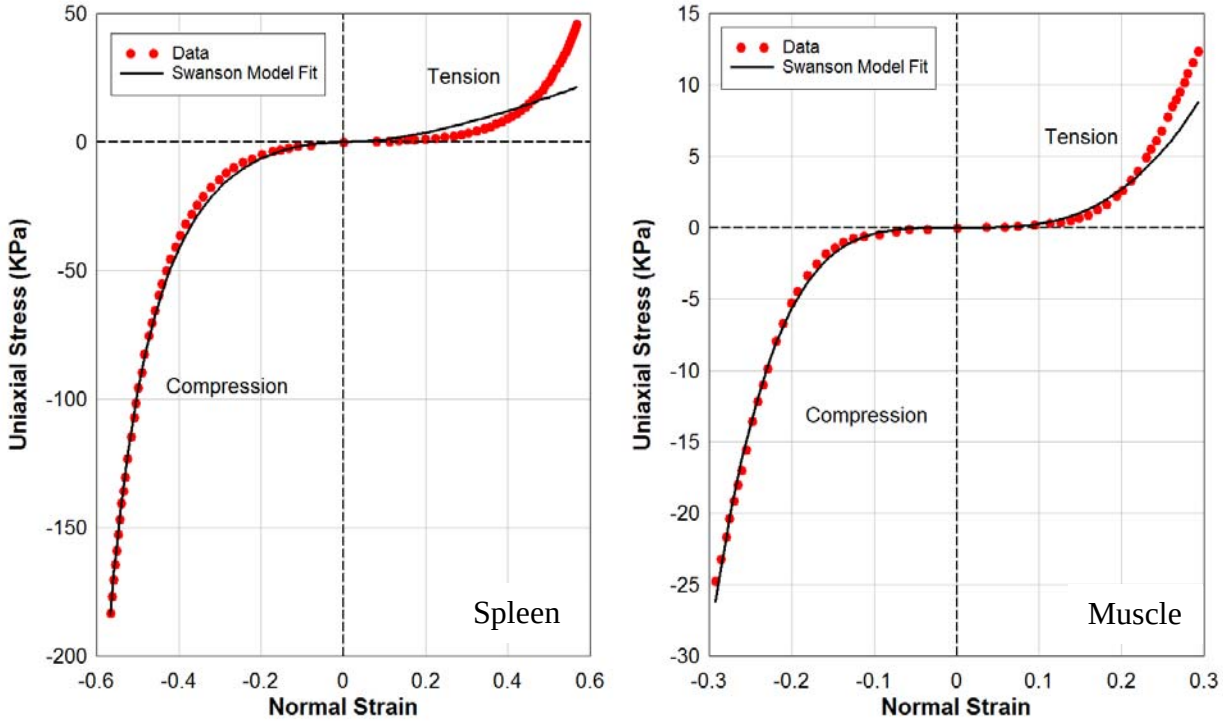

Figure 7. Plots of Swanson model fit with experimental data for Spleen and Muscle.

The failure model representation for bone employs a strain-to-failure fracture model. This model introduces a damage variable *D* that is defined according to the relation

$$D(x,t) = \int_0^t \frac{d\varepsilon^p}{\varepsilon_f^p}, \tag{9}$$

where ε^p is the equivalent plastic strain, continuously updated at each time step, and ε_f^p denotes the critical value of equivalent plastic strain at fracture. $D = 0$ denotes undamaged material whereas failure is considered to have occurred whenever D reaches the value of 1. The damage variable is calculated for each material point in the bone at every time step, degrading both the plastic yield strength Y and fracture stress σ_f of the material in the following manner:

$$Y(x,t) = Y_o[1 - D(x,t)] \text{ and } \sigma_f(x,t) = \sigma_f^o[1 - D(x,t)], \tag{10}$$

where Y_o and σ_f^o denote values of yield and fracture stress, respectively, for undamaged bone. For the material properties of bone, we have selected data reported by Carter [22] in which Y_o = 95 MPa, σ_f^o = 77.5 MPa, and ε_f^p = 0.016. The complete list of material property values for bone and other materials comprising the torso model is presented in Table 2.

The spinal cord consists principally of white matter similar to that found in the brain. As such, we modeled the spinal cord as a viscoelastic material employing the same model and parameters we have used in the past to define white matter. Specifically, the deviatoric response of

the spinal cord is represented by a 3-term Maxwell viscoelastic constitutive model. The time-dependent shear modulus of this material assumes the form:

$$G(t) = G_\infty + (G_o - G_\infty)e^{-\beta t}, \tag{11}$$

where t denotes time, G_o is the short-term shear modulus, G_∞ is the long-term modulus, and β denotes a viscous decay constant for the material. These parameters were taken from the paper by Zhang et al. [21] for white matter and are listed in Table 3 for the spinal cord.

The constitutive model representations for the materials comprising the head-neck model, including white and gray brain matter, falx and tentorium membranes, and scalp-muscle have been described in the paper by Taylor, et al. [5] and are not presented here.

Table 1. Swanson model parameters of selected materials comprising the torso model.

Material	A_1 (KPa)	B_1 (KPa)	C_1 (KPa)	P_1	Q_1	R_1	$\sigma_{fracture}$ (KPa)	$\varepsilon_{fracture}$
Lung	3.66	-2.09	8.0	0.47	0.78	2.01	4.6	0.4
Heart	-605.6	1089.6	-454.0	1.0	0.5417	1.0	10.4	0.23
Liver	-22.19	204.67	-182.37	30.5	0.948	9.452	1850	0.33
Kidney	287.73	569.09	-856.49	1.0	2.672	3.894	4780	0.36
Spleen	-38.26	3.859	35.155	177.57	1.34	0.469	65.0	0.18
Muscle	336.47	340.69	-674.16	1.24	4.44	2.772	10.0	0.2

Table 2. Physical properties of materials comprising the torso model.

Material	Density (g/cc)	Bulk Modulus (MPa)	Shear Modulus (MPa)	Yield Stress (MPa)	$\sigma_{fracture}$ (MPa)	$\varepsilon_{fracture}$
Bone	1.21	4762	3279	95	77.5	0.016
Intervertebral Discs	1.0	8.33	1.79	--	77.5	--
Costal Cartilage	1.0	8.33	1.79	--	77.5	--
Larynx	1.0	8.33	1.79	--	77.5	--
Vasculature/Blood	1.05	T-B fit	--	--	--	--
Airways/Air	1.22e-3	See Fig. 4	--	--	--	--
Lungs	0.7	150	Table 2	--	10.0	--
Liver	1.06	280	Table 2	--	10.0	--
Kidneys	1.1	276	Table 2	--	10.0	--
Spleen	1.1	276	Table 2	--	10.0	--
Heart	1.0	380	Table 2	--	10.0	--
Muscle	1.2	34.8	--	--	10.0	--
Stomach	1.05	480	0.096	--	10.0	--

Stomach Contents	1.0	T-B water		--	--	--
Spinal Cord	1.04	T-B fit	Table 3	--	--	--
Cerebrospinal fluid	1.004	T-B fit	--	--	--	--
Abdominal Cavity Contents	1.2	34.8	5.88	--	10.0	--
Thyroid	1.2	34.8	5.88	--	10.0	--
Skin	1.2	34.8	5.88	--	10.0	--
Kevlar® Plate	1.44	2084	TI fit	--	--	--
Chest Armor Foam	0.136	4.44	3.33	--	77.5	--
9 mm FMJ Bullet	11.689	45826	8600	54	460	--

Table 3. Viscoelastic material parameters for the spinal cord.

	Short-term Shear Modulus G_o (KPa)	Long-term Shear Modulus G_∞ (KPa)	Decay Constant β (sec^{-1})
Spinal Cord	41.0	7.8	40

3. SIMULATION METHODS

Blast and ballistic projectile impact simulations were performed using the shock wave physics code CTH [4]. CTH is an Eulerian finite-volume computer simulation code that is capable of tracking 90+ materials simultaneously, simulating their interactions as they undergo impact, blast loading, and penetration. This code adequately captures the fluid-solid interactions that occur between blast waves and the human torso and head-neck-torso models. CTH possesses an extensive array of constitutive models with which to represent bone, biological tissue, projectile materials, and both the ambient and pressurized air used in the simulations. For our specific applications, we created a specific version of CTH that we modified by adding the Swanson hyperelastic constitutive model for representation of the torso materials listed in Table 1.

We conducted various simulations of direct blast exposure and projectile impact on our torso model both without and with the addition of notional body armor. For the purpose of testing the newly developed torso and head-neck-torso models, blast conditions were selected that were identical to those conditions used previously in simulations on the head-neck model [5]. These blast conditions are representative of those that a warfighter might experience during exposure to an IED detonation. In particular, we employed a blast pulse that would be generated from a spherical 2.3 kg charge of Composition-4 (C-4) located 2.3 meters from the torso model. This explosion produces an air blast of 260 kPa (2.6 bars) overpressure with a pulse width of 2.0 msec as it encounters the torso model.

To reduce computational overhead, we approximate the blast wave produced by a detonating explosive without explicitly including the detonation event in our simulations. In this case, we perform these simulations by positioning the torso model within an environment of air at ambient conditions. We create the blast wave by introducing a slab of energized air, located approximately 36 cm from the torso at time zero. The back face of the air slab is fixed by a rigid boundary whereas the boundary at the front face of the slab, closest to the torso model, is removed for times greater than zero. When this occurs, air mass flows from the energized slab, creating a pressure pulse that propagates in the direction of the torso model. The amplitude and pulse width of the blast wave is determined by setting the energized air to predefined conditions of energy, pressure, and slab thickness. By the time the pressure pulse reaches the torso, its amplitude has degraded to a specified magnitude, in this case 260 kPa gauge pressure, displaying a blast pulse similar to the classical Friedlander waveform (see Fig. 8) [23].

Ideally, we would validate our torso model and simulation methodology against forensic wound data obtained from battlefield injuries due to blast and ballistic projectile impact. Since we are still in the process of collecting this data, our validation task has yet to be accomplished. With that said, we can still demonstrate our modeling and simulation approach to wound injury investigation and personal armor assessment for the torso. As such, the reader is cautioned that the results we present here are for illustrative purposes and, at this time, are not meant to provide quantitative assessments of wound dynamics or armor assessment. One exception here is the head-neck portion of the head-neck-torso model, which has undergone validation as described in the paper by Taylor et al. [5].

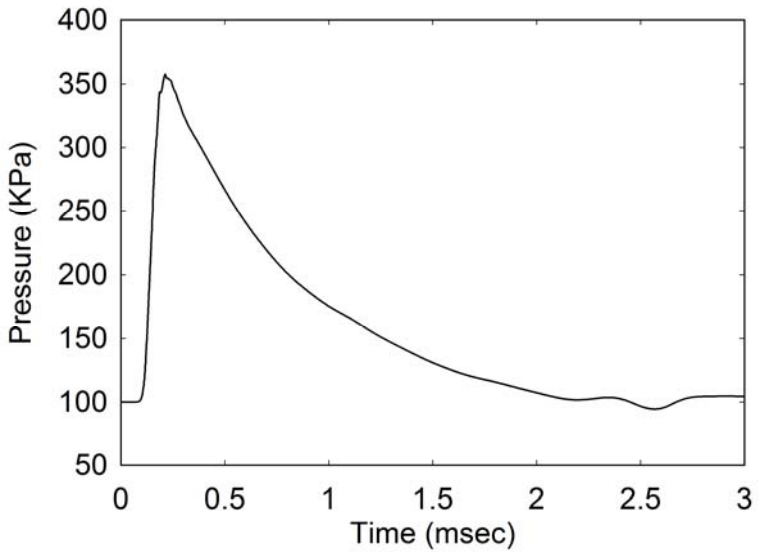

Figure 8. Simulated 260 KPa (Gauge) Blast Pulse.

Notional torso armor was created to demonstrate the capability for relative merit assessment. Our chest armor model is composed of a 1.0 cm thick Kevlar® shell in the blast simulations and a 1.5cm thick Kevlar® shell in the ballistic projectile impact simulations. The projectile used in these simulations is a mock representation of a 9 mm full metal jacket (FMJ) bullet. This representation captures the geometry and mass of a 9 mm FMJ bullet while simplifying its composition to that of a single-material projectile. The Kevlar® shell was represented by a Mie-Gruneisen EOS and the Transverse Isotropic (TI) constitutive model [24] describing its deviatoric response. The TI model parameters for this material are proprietary and, as such, are not listed here. Equation-of-state and constitutive model representations for the chest armor backing foam and the 9 mm FMJ bullet are listed in Table 2.

4. SIMULATION RESULTS

We have conducted a variety of blast and projectile impact scenarios to both the unprotected and protected Sandia Torso model in order to demonstrate the utility of our modeling and simulation toolset. The specific simulations performed are shown in Table 4.

Table 4. Simulation Matrix.

Simulation	Torso Unprotected	Torso With Armor and Padding	Torso With Armor Without Padding	Head-Neck-Torso Unprotected
Frontal Blast	**X**	**X**	**X**	**X**
Side Blast	**X**			
Rear Blast	**X**			
Projectile Impact		**X**	**X**	

In order to maintain an acceptable page length for this report, we present results from selected simulations. These results are presented in the following sections.

4.1 Blast Loading

As mentioned in Section 3, we approximate the blast wave produced by a detonating explosive without explicitly modeling the detonation event. This approach significantly reduces computational time without sacrificing simulation accuracy. We have focused on simulating injury scenarios that introduce blast waves that correlate with the threshold conditions for lung damage, as defined by the modified Bowen criteria for lung injury [25]. In the following two subsections, we present the results of blast simulations for the unprotected and protected torso.

4.1.1 Unprotected Torso

In this section, we present the simulation results for the unprotected torso model when exposed to a frontal blast of 260 kPa in magnitude. Figure 9 contains an image sequence depicting the progression of the blast as it interacts with the torso. This interaction creates a transmitted wave that propagates through the model, inducing internal wave reflections and transmissions in the torso that are influenced by the impedance differences between the different tissue types.

On close inspection of Figure 9, one can notice that the magnitude of the transmitted wave, as it propagates through the torso, is magnified or reduced depending on whether it encounters a material of high mechanical impedance or one of low impedance, respectively. For the sake of clarity, mechanical impedance is defined as the material's mass density multiplied by its dilatational sound speed, i.e.,

$$Mechanical\ Impedance = \rho c_d \ . \tag{12}$$

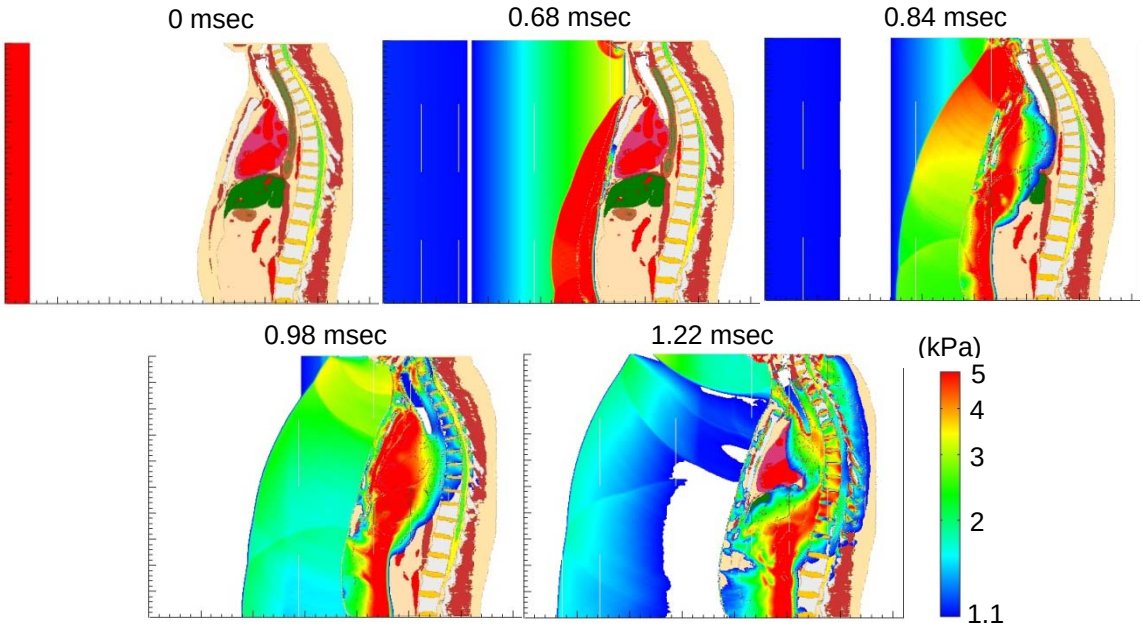

Figure 9. Pressure time-progression sequence of a 260kPa frontal blast exposure to the unprotected torso.

For quantitative investigation and comparative analysis, we monitor the history of a variety of physics variables (stress, strain, strain rate, strain energy, etc.) recorded at specific Lagrangian tracer points placed at various locations throughout the torso. We defer further discussion of these results until Section 4.1.2 in which we present a comparison between results from the unprotected and protected torso blast scenarios.

4.1.2 Torso with Prototype Armor

This section summarizes the results of the protected torso when exposed to a 260 kPa frontal blast. Figure 10 contains the image sequence depicting the progression of the blast as it interacts with the torso protected by chest armor with foam padding (yellow).

In previous armor assessment analyses, we have found that mitigation of the transmitted blast wave as it propagates through the chest armor depends highly on the mechanical impedance of the foam padding. To examine this phenomenon further, we have conducted blast simulations of the torso protected by chest armor without the foam padding in which the hard armor shell is offset from the body by a maximum of 2.5 cm at its center, only touching the torso at the lateral edges of the shell as a result of its cylindrical curvature. Although hypothetical, this arrangement is meant to approximate chest armor possessing padding of minimal mechanical impedance. The time progression pressure wave sequence of this simulation is shown in Figure 11.

In this case, the blast wave reflects off the armor shell generating a transmitted wave which propagates through the shell, transmitting a low magnitude pressure wave in the air between the shell and the torso. As in the shell and pad armor case, differences in mechanical impedance between the various materials of the chest armor and torso induce internal wave reflections and transmissions in the torso.

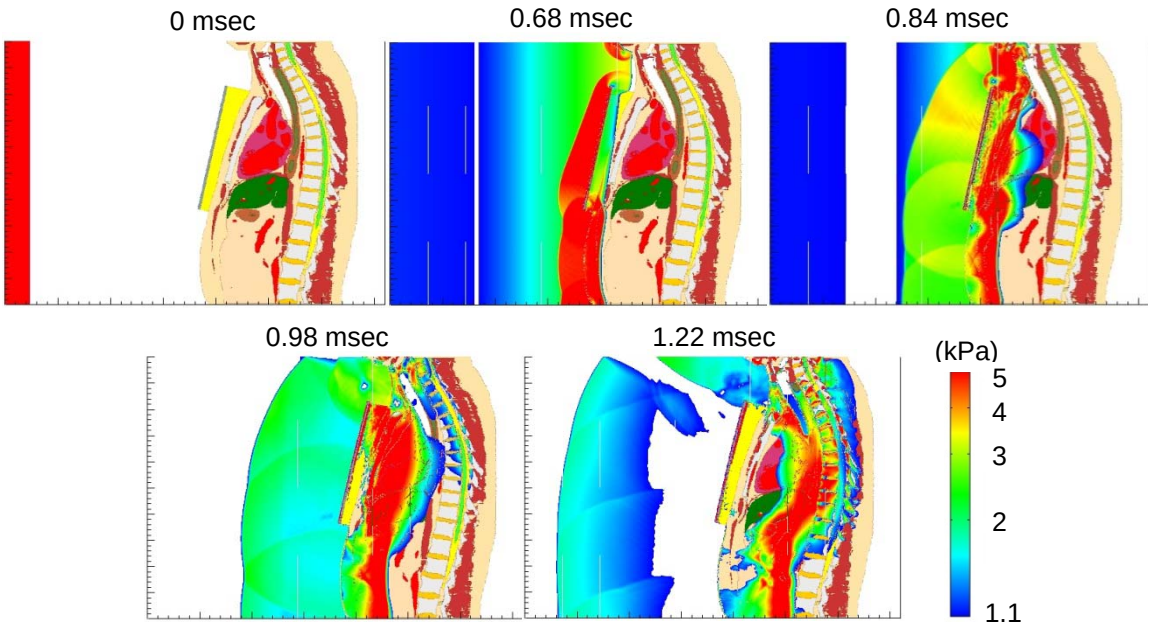

Figure 10. Pressure time-progression sequence of a 260kPa frontal blast exposure to the torso protected by chest armor with padding.

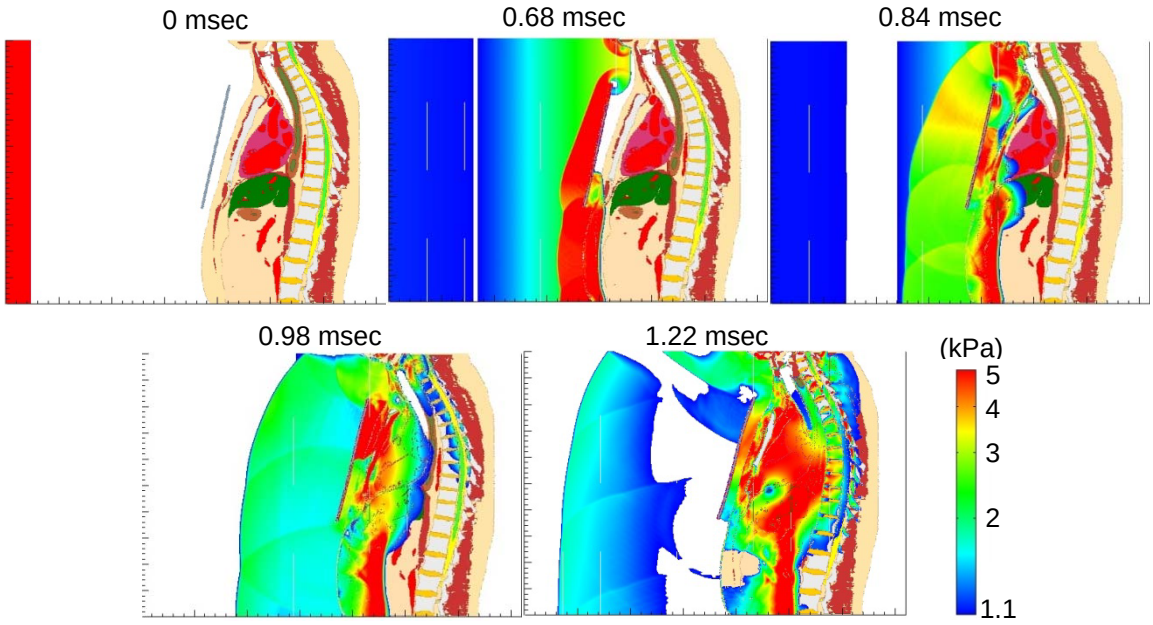

Figure 11. Pressure time-progression sequence of a 260kPa frontal blast exposure to the torso protected by offset chest armor without padding.

Comparing the progression of the pressure wave as it transits the torso (see Figures 10 and 11), one can see that the armor without padding delays the advance of the wave into the torso. That is, the torso is subjected to a delayed pressure pulse formed once the air between the armor shell and torso is pressurized by the blast wave as it enters the air gaps at the top and bottom of the plate.

Figures 12-15 show the pressure history plots of Lagrangian tracer points placed within the heart, right lung, left lung, and liver. These plots show the pressure at those points throughout the duration of simulations. Note that the addition of armor creates various changes in the pressures seen within the various organs. Notice that the addition of armor, with or without padding, causes an increase in the peak pressures within the heart and liver over the unprotected case. However, the increase in peak pressure within the heart and liver is accompanied by a decrease in loading rate. The increase in peak pressure due to the presence of the armor is not seen in the lungs. Figures 13 and 14 show that the armor with padding does not change the pressure magnitude or its rate of loading in the lungs; however, there is an extension in the pulse width over that for the unprotected torso. Interestingly, the armor without padding does reduce the peak pressure magnitudes in the lungs. Here, however, there is an extension in the pulse width, even beyond that for the armor with padding.

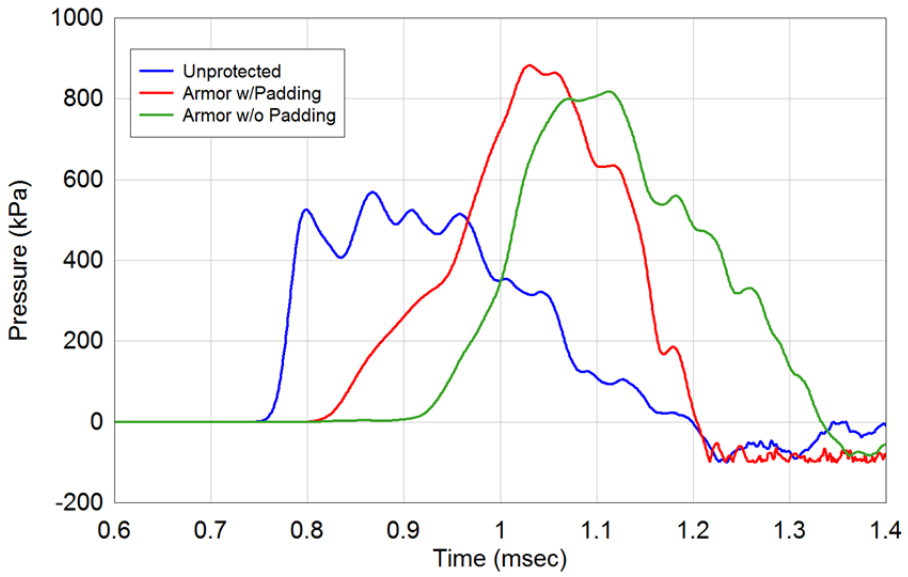

Figure 12. Comparison of heart pressure histories between unprotected, protected with chest armor padding, and protected without armor padding.

Figures 16-19 contain plots of the associated von Mises (shear) stress histories for the Lagrangian points in the heart, lungs, and liver. For all of these organs, the unprotected case displays the minimal amount of increase in von Mises shear stress relative to both of the armor protected cases. The greatest shear stress levels occur for the case of armor protection with padding. The most likely explanation for this result lies with the fact that the armor materials (i.e., the hard shell and foam padding) possess nontrivial shear strengths that permit the formation of shear waves in the armor itself during blast loading that are transmitted into the torso by means of direct contact through the padding. These shear waves induce significantly higher shear loads in the torso than would otherwise be experienced during blast loading in the unprotected case. Also, when the foam padding is absent, as in our case of armor without padding, the shear stress levels in the torso are greatly reduced since there is no longer a direct conduit for transmission of the shear waves formed in the armor plate to pass through to the torso.

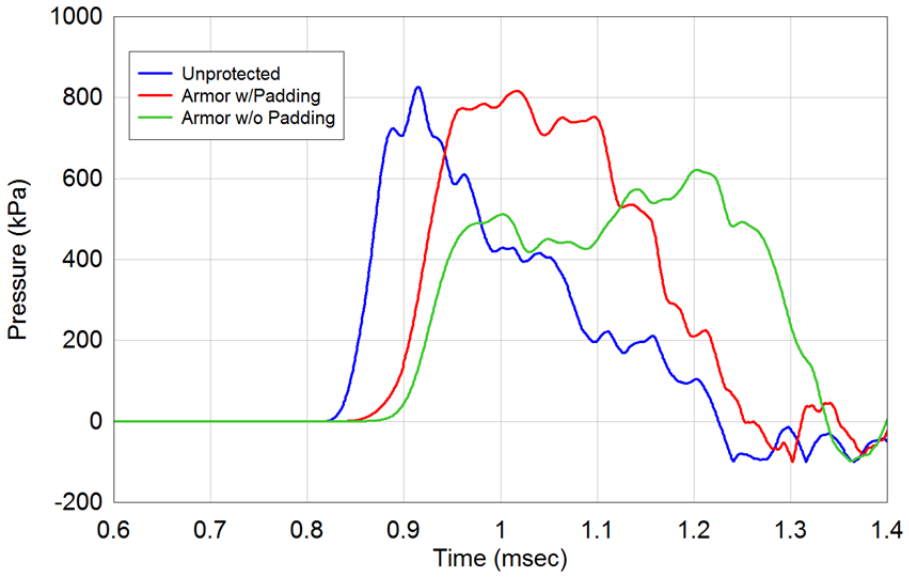

Figure 13. Comparison of right lung pressure histories between unprotected, protected with chest armor padding, and protected without armor padding.

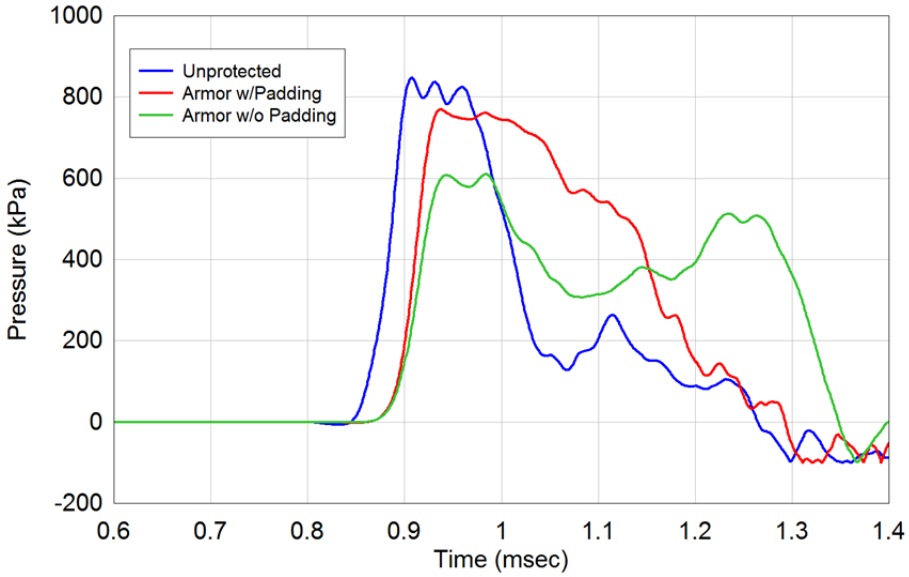

Figure 14. Comparison of left lung pressure histories between unprotected, protected with chest armor padding, and protected without armor padding.

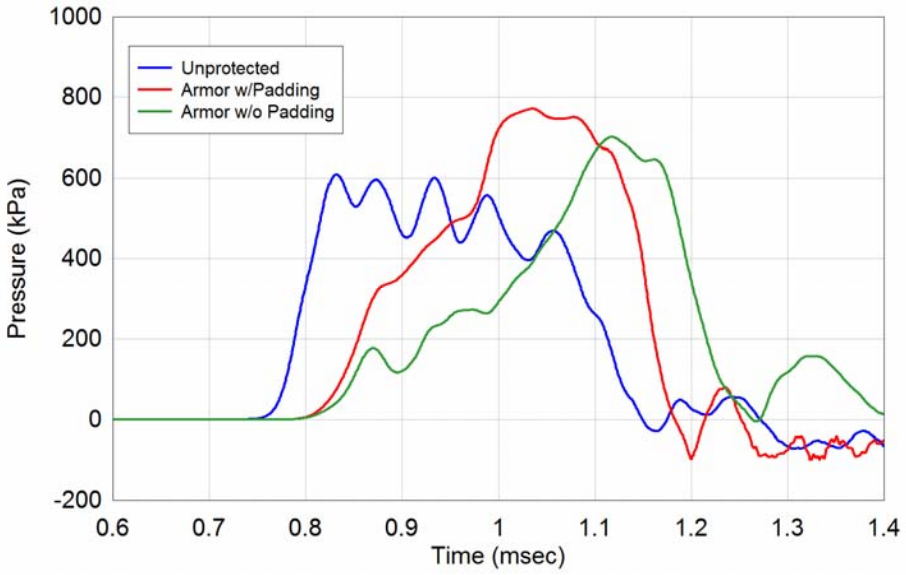

Figure 15. Comparison of liver pressure histories between unprotected, protected with chest armor padding, and protected without armor padding.

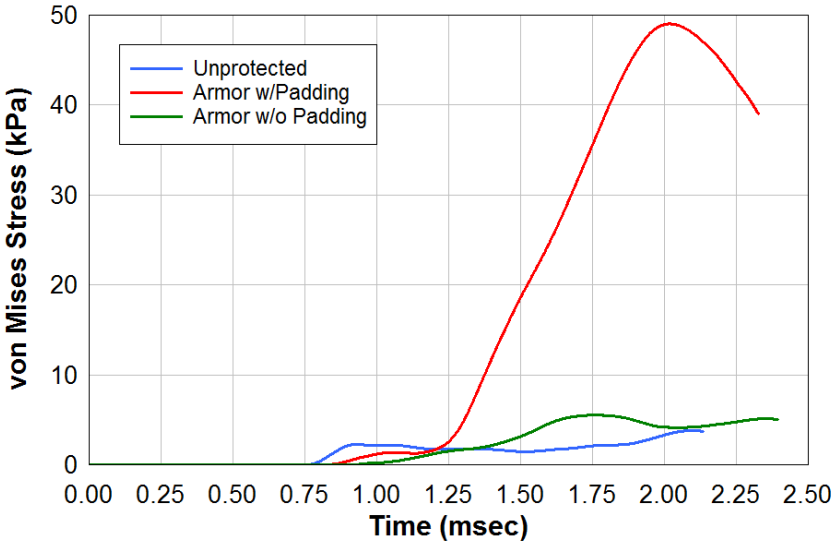

Figure 16. Comparison of von Mises (shear) stress histories in the heart between unprotected, protected with chest armor padding, and protected without armor padding.

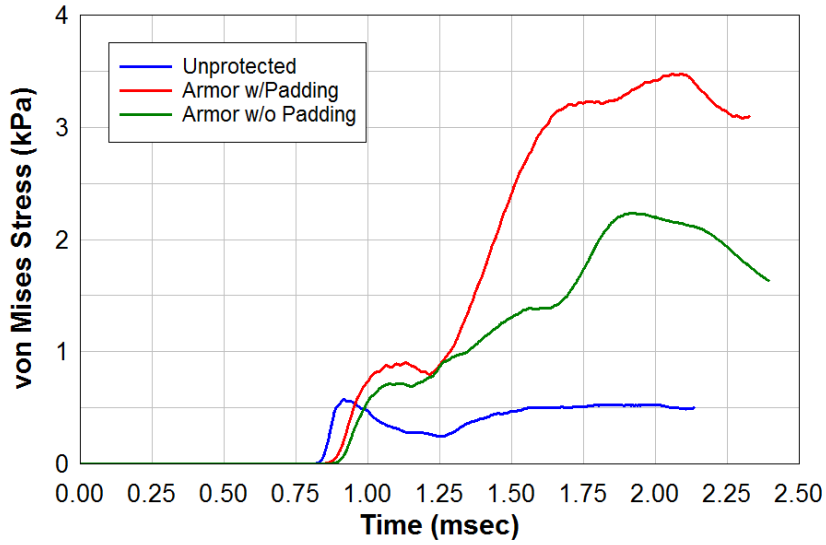

Figure 17. Comparison of von Mises (shear) stress histories in the right lung between unprotected, protected with chest armor padding, and protected without armor padding.

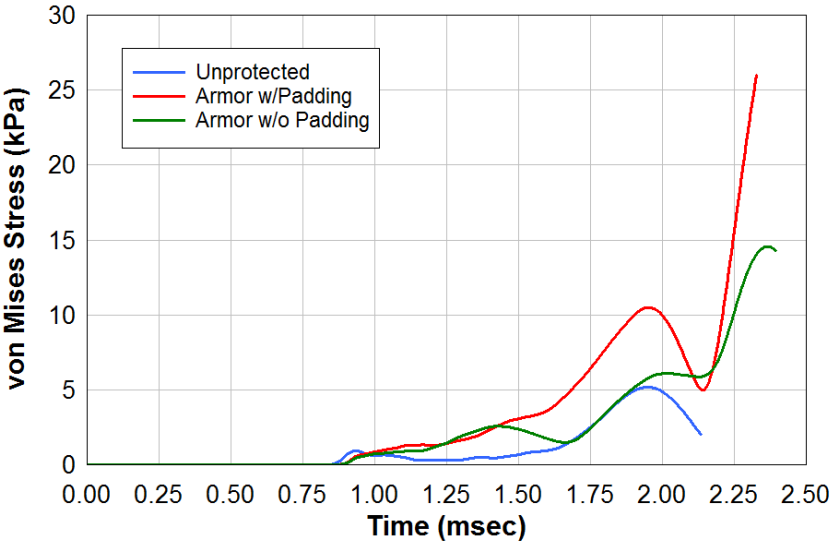

Figure 18. Comparison of von Mises (shear) stress histories in the left lung between unprotected, protected with chest armor padding, and protected without armor padding.

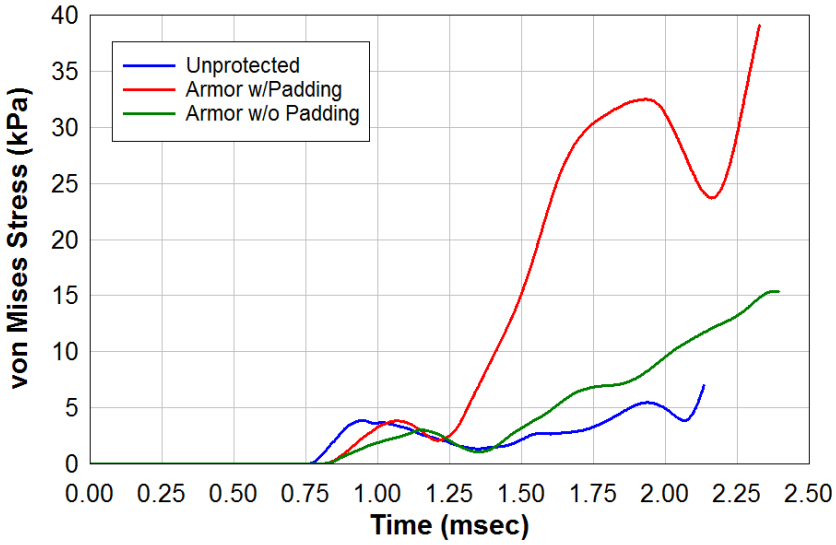

Figure 19. Comparison of von Mises (shear) stress histories in the liver between unprotected, protected with chest armor padding, and protected without armor padding.

Since the chest armor we have modeled in these examples is notional, our comparison of the pressure and shear stress histories in Figures 12-19 should be viewed only as a demonstration that one can use a virtual approach to assess armor designs. Since we have yet to complete validation of the torso model, armor assessment with our human torso model can only be conducted in a relative manner. That is, if the pressure and shear stress magnitudes are reduced by armor 1 relative to armor 2, then one can conclude that armor 1 provides superior protection.

4.1.3 Head-Neck-Torso

In this section, we present simulation results for the unprotected head-neck-torso (H-N-T) model, exposed to the same 260 kPa frontal blast conditions experienced by the torso model in section 4.1.2. Although it might appear beneficial to use a more complete human model to investigate wound injury and armor protection for the torso region, the computational overhead in employing such a model can be prohibitively expensive in both computer execution time and mass storage requirements. This same consideration can also be made when simulating injuries to the head using a separate head-neck model. Our intent in this instance is to assess whether simulations of wound injury to the torso can be conducted with a truncated human model of the torso or require a more complete human model, such as that employed here representing the head, neck, and torso together.

Figure 20 contains an image sequence depicting the progression of the blast as it interacts with the H-N-T model. As with the torso model, the blast wave creates a transmitted wave that propagates through the H-N-T model, inducing internal wave reflections and transmissions that are influenced by the impedance differences between the different tissue types comprising the model.

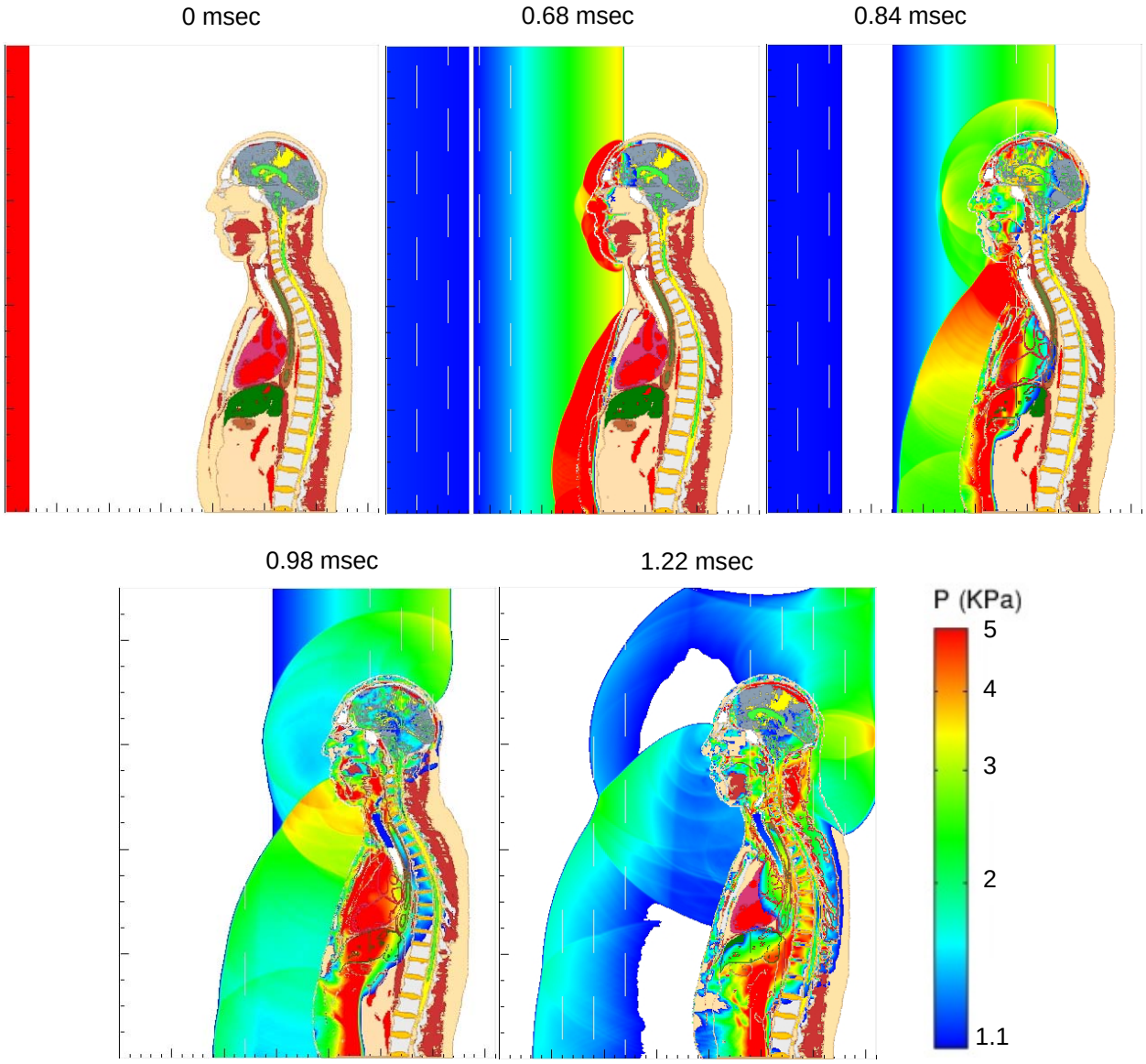

Figure 20. Pressure time-progression sequence of a 260kPa frontal blast exposure to the unprotected head-neck-torso.

Figures 21-24 present a comparison of the pressure and von Mises stress histories for the heart, lungs, and liver predicted by simulations using the head-neck-torso model versus the torso model separately. The reader should note that the torso model simulation predicts both pressure and von Mises stress histories almost identically to that predicted using the comprehensive head-neck-torso model. The only distinction between the two predictions is the extent of simulated time to which the torso model simulation was able to achieve before spurious pressure waves caused a non-recoverable error in the simulation. These spurious waves are the result of artificial conditions imposed on the upper boundary of the torso model to approximate the presence of an otherwise absent neck and head. Without this condition, the blast-induced intrathoracic pressure waves would cause the upper contents of the torso to eject through the upper boundary of the

truncated torso. The spurious pressure waves themselves are not of sufficient magnitude to cause noticeable inaccuracies in the simulation (as witnessed in the plots of Figures 21-24) and would be an acceptable annoyance if they would not cause non-recoverable errors to occur in the calculation. However, without the ability to execute the blast simulation out to at least 3 milliseconds of simulation time, the torso model simulations would be incomplete since they would miss the late-time increase in von Mises stress in the heart, right lung, and liver.

The usefulness of the combined head-neck-torso model lies with the advantage it provides researchers when investigating wound injury and personal armor protection for areas of the human body that extend beyond an isolated region. For example, the investigation of pressure wave propagation through the body that may induce brain injury mechanisms as a result of blast loading to the torso.

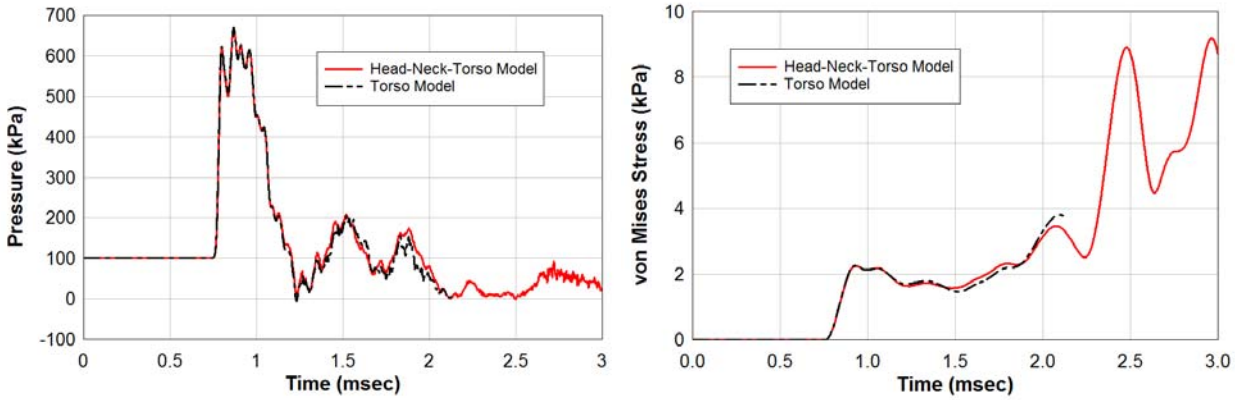

Figure 21. Heart pressure and von Mises stress history comparisons between simulation predictions using the full head-neck-torso model versus the torso model.

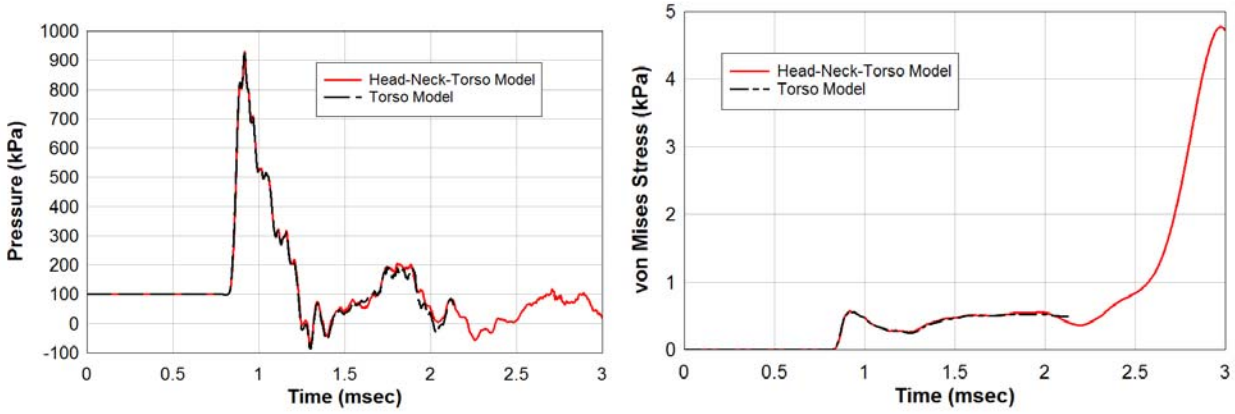

Figure 22. Right lung pressure and von Mises stress history comparisons between simulation predictions using the full head-neck-torso model versus the torso model.

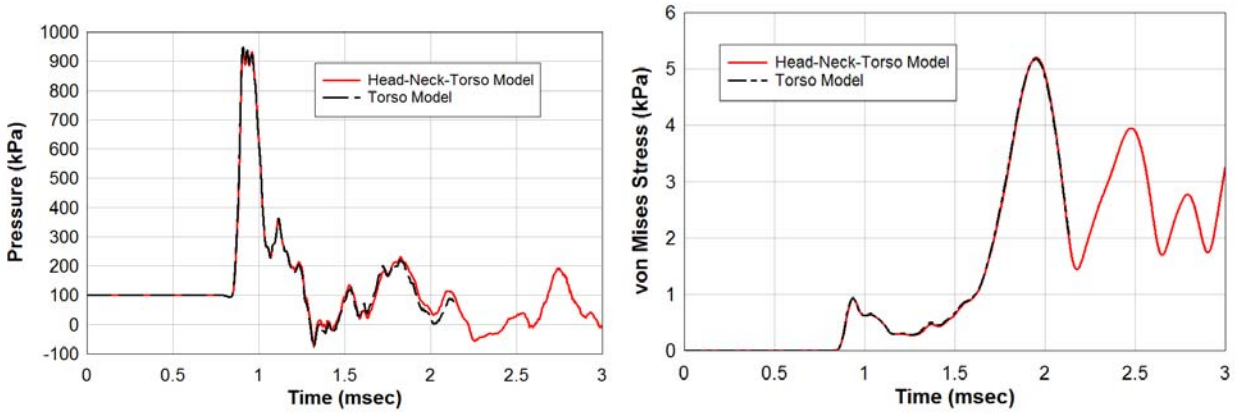

Figure 23. Left lung pressure and von Mises stress history comparisons between simulation predictions using the full head-neck-torso model versus the torso model.

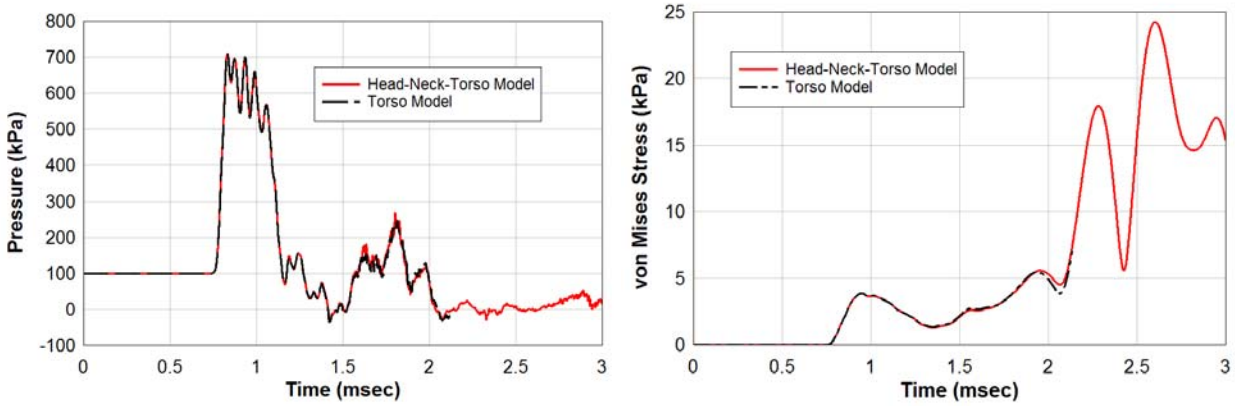

Figure 24. Liver pressure and von Mises stress history comparisons between simulation predictions using the full head-neck-torso model versus the torso model.

4.2 Ballistic Projectile Impact

In this section, we demonstrate the value of the Sandia torso model in analyzing behind-armor blunt trauma as a result of a ballistic projectile striking chest armor. Here, we use similar prototype armor that was described in Section 4.1.2 for chest protection from frontal insult. However, for these bullet impact scenarios, we have increased the armor plate to a thickness of 1.5 cm to ensure that the bullet is arrested by the armor plate. The projectile used in this example is a facsimile of a 9x19 mm parabellum full metal jacket (FMJ) round traveling at a velocity of 370 m/sec, typical of Uzi submachine gun bullet velocities.

For this demonstration, we compare the pressures and von Mises (shear) stresses in the torso at specific locations in life-critical organs resulting from use of chest armor with and without padding. It is of no value to consider the unprotected case since our simulations have shown that

the 9 mm projectile penetrates the torso, piercing the heart, most certainly causing serious, if not fatal, injury. To investigate behind-armor blunt trauma, we construct the armor plate to arrest the projectile and analyze the resulting stress loads experienced by the life-critical organs as a result of the dilatational and shear waves generated during the impact process.

Figures 25 and 26 display time-sequenced pressure profiles that result from the 9 mm FMJ striking the chest armor with and without foam pad backing, respectively.

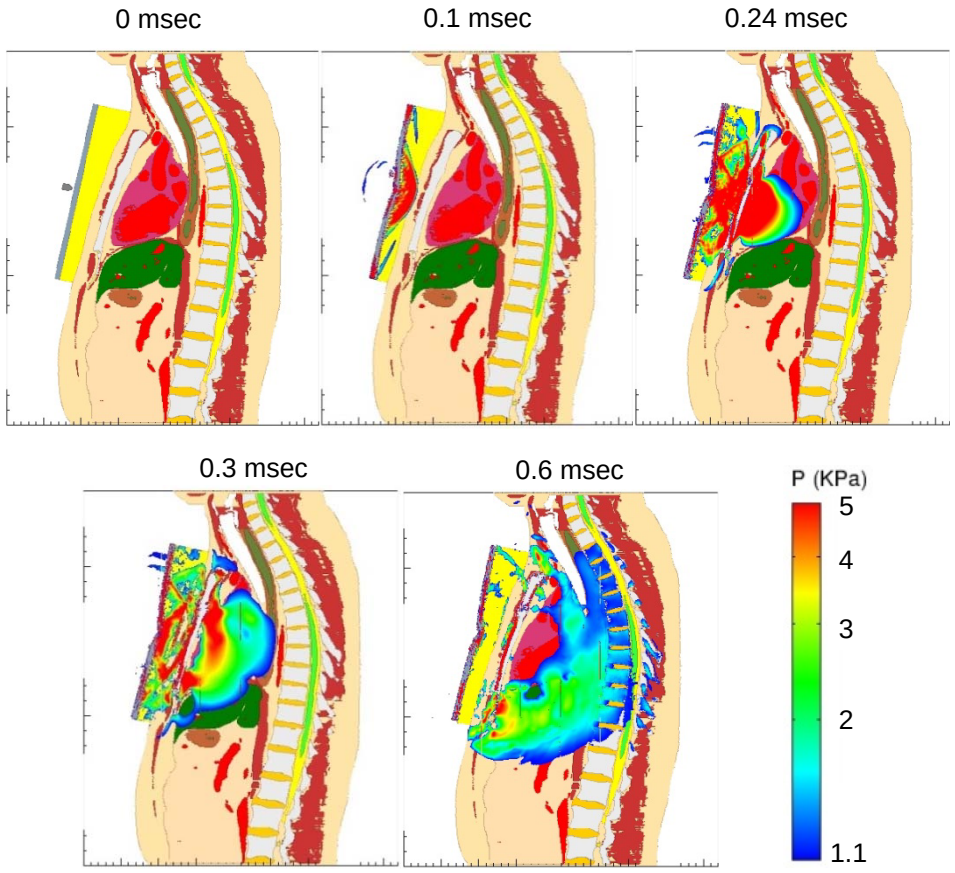

Figure 25. Pressure time-progression sequence of a 9 mm ballistic projectile impact to the torso protected by chest armor with padding.

A comparison of the pressure profiles in Figures 25 and 26 demonstrates the protective advantage of armor that is separated by padding of low mechanical impedance. In this case, we compare chest armor backed by foam padding of realistic impedance (Figure 25) with armor backed by padding possessing asymptotically small impedance, i.e., that of air (Figure 26). Specifically, the presence of the foam padding permits transmission of the compression and shear waves, formed in the armor as a result of the impact, to pass directly into the torso at magnitudes and speeds higher than what would be possible in absence of the padding.

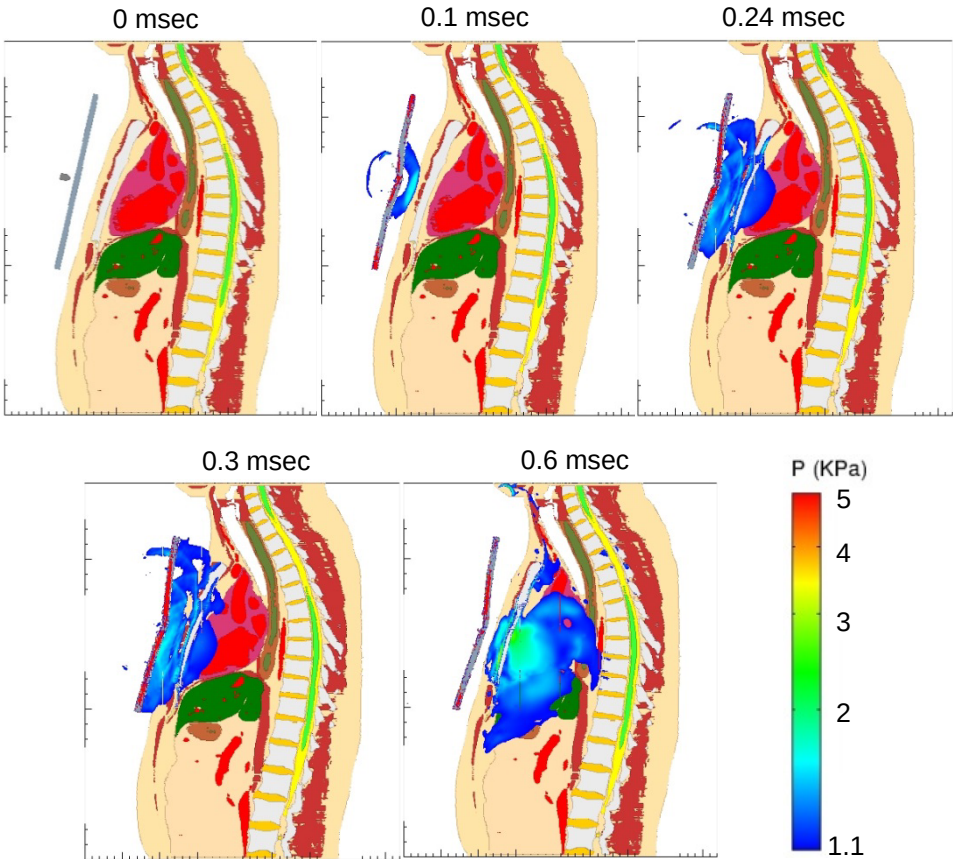

Figure 26. Pressure time-progression sequence of a 9 mm ballistic projectile impact to the torso protected by offset chest armor without padding.

Our observations are corroborated by the pressure histories, plotted in Figures 25-30, for the heart, lungs, and liver, respectively. The most obvious difference between the two armor configurations can be seen in the pressure history plots for the heart and liver, Figures 27 and 30, respectively. In these instances, the pressure loads to the heart and liver are all but eliminated in the armor system possessing padding of minimal impedance.

The pressure histories for the lungs (Figures 28 and 29) show significant pressure reduction with the zero impedance padding but, since the armor shell touches the torso at its lateral edges, some pressure pulse is transmitted into the torso and the lungs which underlie the contact edges.

Plots of the von Mises shear stress, as seen in Figures 31-34 for the heart, lungs, and liver, are consistent with the trends suggested by the pressure histories in those organs. That is, the padded armor permits significantly higher shear stress levels to occur in both the heart and liver than in the case of armor without padding (see Figures 31 and 34). However, the shear stress levels in both of the lungs, as seen in Figures 32 and 33, show far less dependence on the existence of the foam padding. As mentioned above, we feel that this is due to the fact that the armor shell touches the torso at its lateral edges, thereby permitting shear wave transmission into the torso and the lungs which underlie the contact edges. This observation suggests that if we could eliminate contact between the armor and the torso altogether, we could realize optimal protection from the armor.

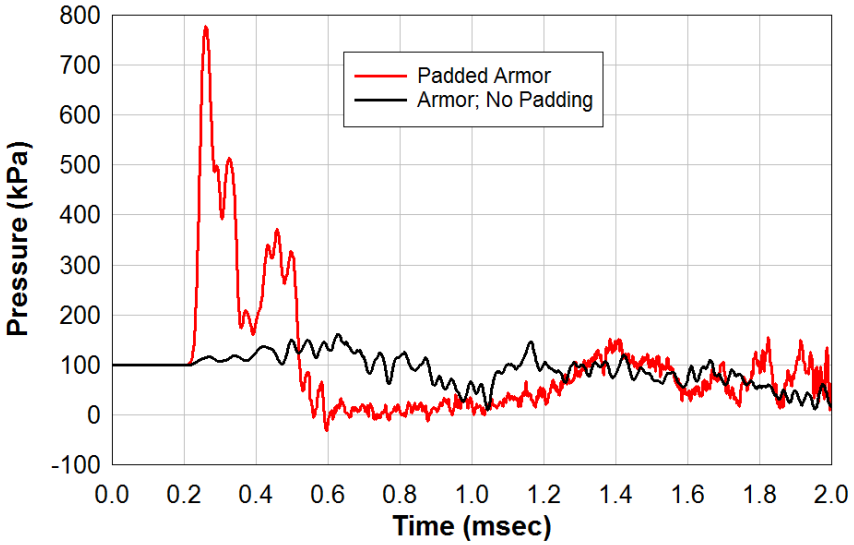

Figure 27. Comparison of heart pressure histories between torso protection with chest armor padding versus armor without padding.

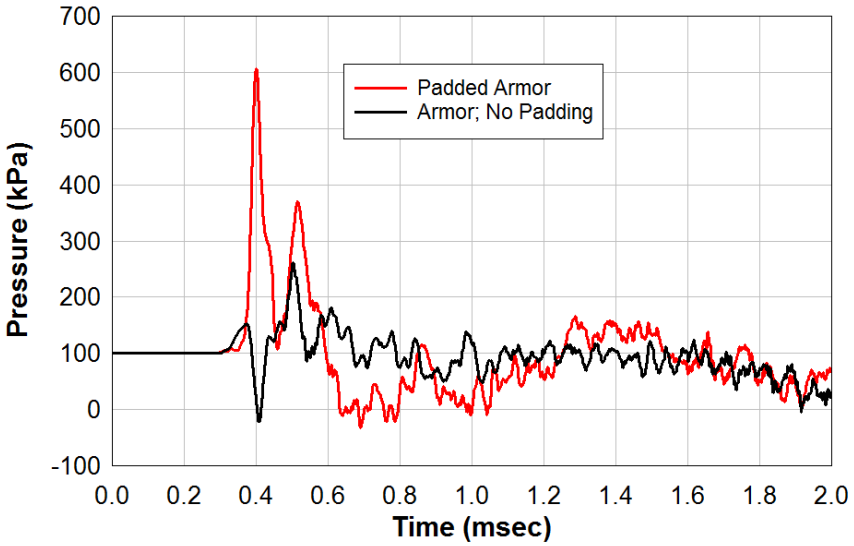

Figure 28. Comparison of right lung pressure histories between torso protection with chest armor padding versus armor without padding.

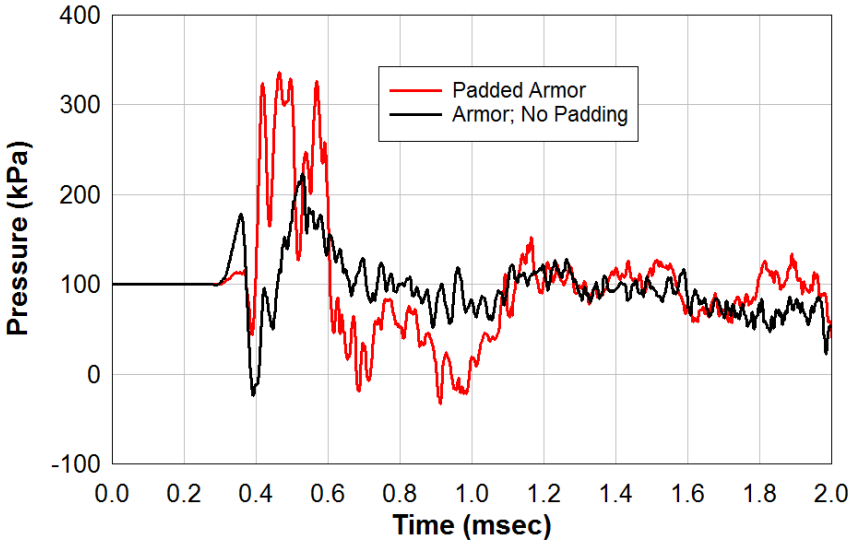

Figure 29. Comparison of left lung pressure histories between torso protection with chest armor padding versus armor without padding.

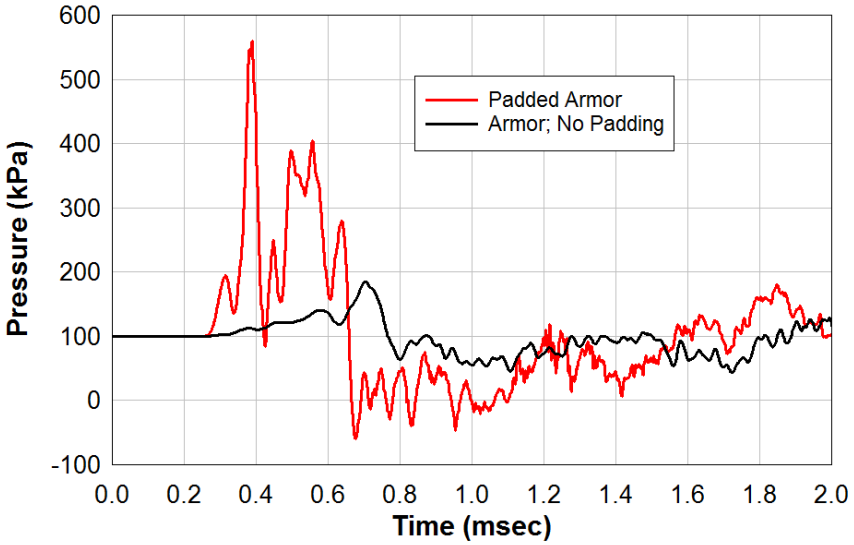

Figure 30. Comparison of liver pressure histories between torso protection with chest armor padding versus armor without padding.

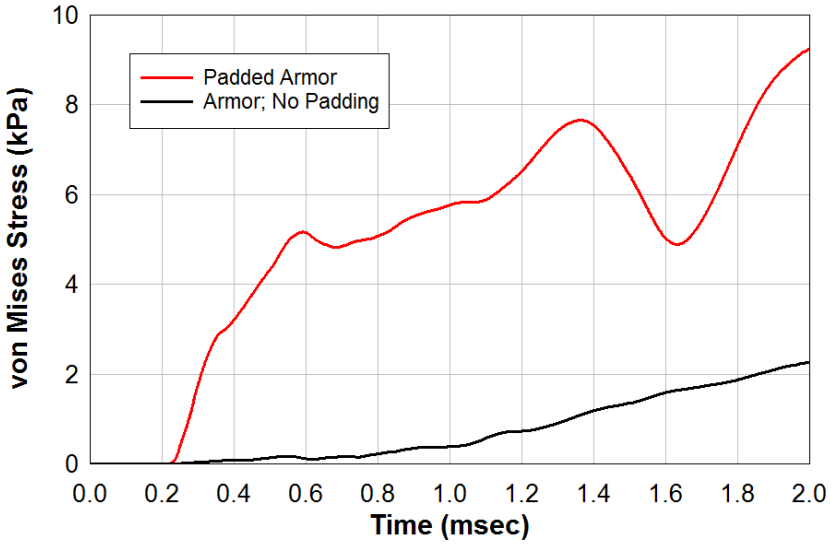

Figure 31. Comparison of von Mises (shear) stress histories in the heart between torso protection with chest armor padding versus armor without padding.

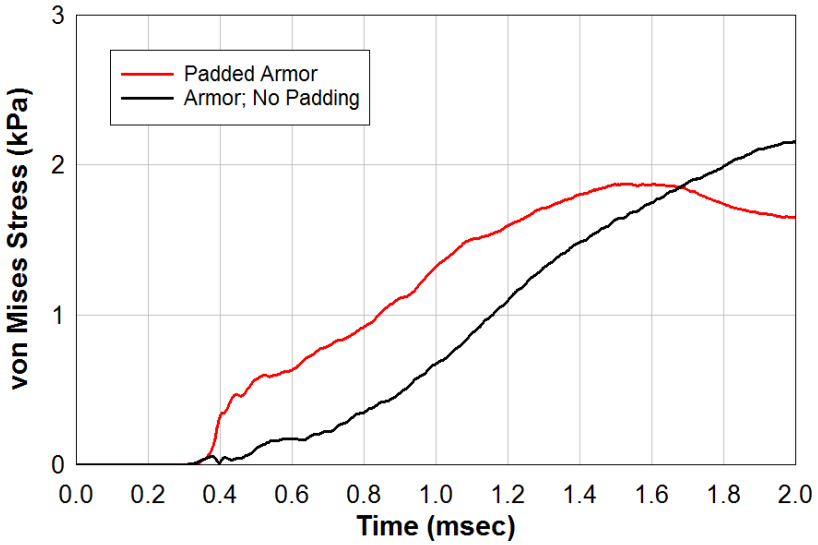

Figure 32. Comparison of von Mises (shear) stress histories in the right lung between torso protection with chest armor padding versus armor without padding.

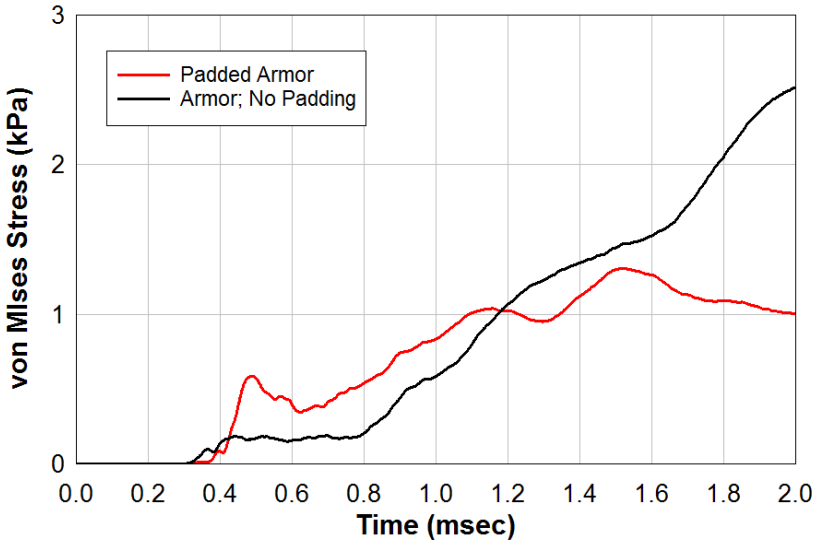

Figure 33. Comparison of von Mises (shear) stress histories in the left lung between torso protection with chest armor padding versus armor without padding.

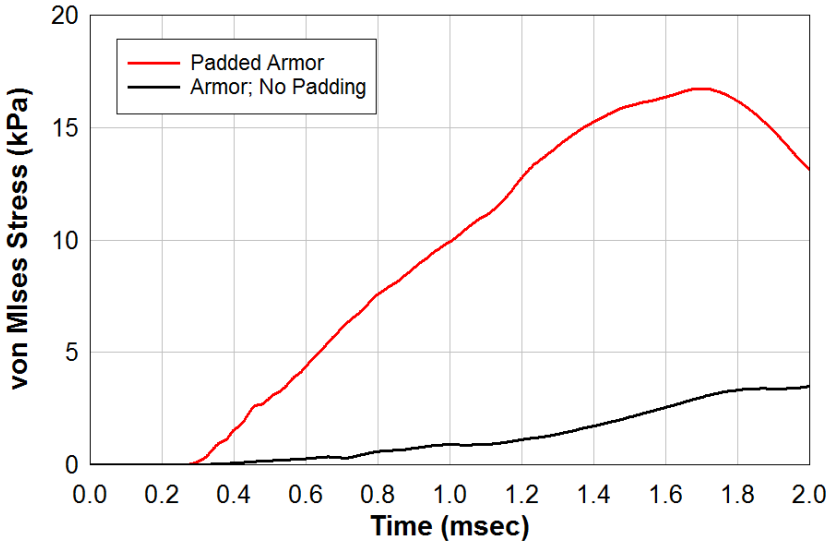

Figure 34. Comparison of von Mises (shear) stress histories in the liver between torso protection with chest armor padding versus armor without padding.

[Blank Page following Section]

5. CONCLUDING REMARKS

During the execution of this Laboratory Directed Research and Development (LDRD) project, we have accomplished the following tasks:

1. Developed high fidelity, finite volume and finite element representations of a human male torso consisting of 19 distinct materials including bone, cartilage, intervertebral discs, vasculature with blood, airways with air, lungs, liver, kidneys, spleen, heart, muscle, larynx, stomach with stomach contents, spinal cord, cerebrospinal fluid (CSF), thyroid, abdominal cavity contents, and fat/skin;
2. Merging of the new torso model with the existing Sandia Head-Neck model to create the Sandia Head-Neck-Torso model for simulation of wound injury and protective armor assessment;
3. Implementation of a modified version of the Swanson hyper-viscoelastic model into the shock physics wave code CTH;
4. Construction of Swanson hyperelastic model representations for torso constituents including the heart, lungs, liver, kidneys, spleen, and muscle;
5. Demonstration of a methodology to simulate wound injury to the head, neck, and torso from blast and ballistic projectile impact;
6. Demonstration of the methodology to simulate personal protective armor assessment for the torso;

   Although not explicitly presented here, this same approach can be used to assess personal armor for the head, neck, and torso for personal armor providing comprehensive coverage of these regions;

Although we have accomplished a great deal during the project, there remains one important task that should be performed before the new Sandia Torso and Sandia Head-Neck-Torso models are ready for use in wound injury investigative research. The task to which we refer is that of model validation. Unfortunately, there exists a significant absence of available battlefield injury data with which to quantitatively validate the torso model specifically, and virtual human models in general. We suspect that this data exists; however, it is extremely difficult to acquire or access due to restrictions imposed on the data by its owners and/or archivists. In our opinion, this issue constitutes the single biggest limitation to modeling and simulation investigations of wound injury and personal armor assessment for the warfighter. Modeling and simulation efforts will continue to be hindered by this limitation until the research community can convince the archivists of warfighter injury data to release the data in order to advance the state-of-the-art of virtual injury scenario investigation.

In absence of wound injury validation data for the torso and head-neck-torso models, one can still perform relative merit assessments of personal protective armor for the warfighter, as we have demonstrated in Section 4. From the examples presented herein, we can draw the following observations:

1. Virtual assessment of personal armor designed for the torso can be conducted using the torso model separately without having to use a more comprehensive model (e.g., the head-neck-torso model);
   -- If assessment of an personal armor ensemble is required (e.g., head and chest armor), then use of the head-neck-torso model is necessary;

2. Armor constructed to protect against ballistic projectile impact can have a deleterious effect on the behind-armor blunt trauma caused as a result of employing foam pad backing with too great of a mechanical impedance {recall definition of impedance in eq.(12)};
   -- This result applies to protection from both blast exposure and ballistic projectile impact;
3. Personal armor can provide greater protection from blast and behind-armor blunt trauma if the armor can be offset from the body with as little contact as possible;
4. In those instances where use of foam pad backing is unavoidable in the personal armor design, internal injury from behind-armor blunt trauma can be minimized by use of foam with as low of mechanical impedance as possible;

Perhaps the greatest advantage of our modeling and simulation approach to wound injury investigation and assessment of personal protective armor is that it can be performed ad infinitum, without extensive use of experimental studies relying on animal models or human cadavers. This statement should not be misconstrued as an endorsement to abandon testing altogether. Testing should continue but with the intent of generating data of use to validate modeling and simulation tools for the investigation of warfighter injury and armor assessment.

As for future work, the modeling and simulation products created from this LDRD project will permit us to pursue new project funding sources within the DOE and DoD. As of the writing of this report, program managers from the Office of Naval Research (ONR) have expressed interest in employing the existing Sandia virtual human models created from this project for warfighter injury assessment as well as funding work to extend the Sandia models to include the urogenital region and lower extremities for mounted warfighter injury investigations.

6. REFERENCES

[1] Roberts, J. C., Biermann, P. J., O-Connor, J. V., Ward, E. E., Cain, R. P., Carkhuff, B. G., and Merkle, A. C., 2005, Modeling nonpenetrating ballistic impact on a human torso.

[2] Roberts, J. C., Merkle, A. C., Biermann, P. J., Ward, E. E., Carkhuff, B. G., Cain, R. P., and O-Connor, J. V., 2007, "Computational and experimental models of the human torso for nonpenetrating ballistic impact," J. Biomech., **40**, pp. 125–136.

[3] 2007, "The National Library of Medicine's visible human project" [Online]. Available: http://www.nlm.nih.gov/research/visible/visible_human.html. [Accessed: 30-Jan-2013].

[4] Hertel, E. S., Bell, R., Elrick, M., Farnsworth, A., Kerley, G., McGlaun, J., Petney, S., Silling, S., and Taylor, P., 1993, "CTH: a software family for multi-dimensional shock physics analysis," Proc. 19th Int. Symp. Shock Waves, **1**, pp. 377–382.

[5] Taylor, P. A., Ludwigsen, J. S., and Ford, C. C., 2014, "Investigation of blast-induced traumatic brain injury," Brain Inj., **28**(7), pp. 879–895.

[6] Hertel, E. S., and Kerley, G. I., 1998, CTH reference manual: The equation of state package, Sandia National Laboratories, Albuquerque, NM.

[7] Brundage, A. L., 2013, "Implementation of Tillotson equation of state for hypervelocity impact of metals, geologic materials, and liquids," Procedia Eng., **58**, pp. 461–470.

[8] Tillotson, J. H., 1962, Metallic equations of state for hypervelocity impact, San Diego, CA.

[9] Cushing, V. J., 1991, Shock induced cavitation.

[10] Siedler, G., and Peters, H., 1986, "Physical properties (general) of sea water," LANDOLT-BORNSTEIN: Numerical data and functional relationships in science and technology, Springer, Berlin, pp. 233–264.

[11] Palaniappan, L., and Velusamy, V., 2004, "Ultrasonic study of human cerebrospinal fluid," Indian J. Pure Appl. Sci., **42**, pp. 591–594.

[12] Nagoya, H., Obara, T., and Takayama, K., 1995, "Underwater shock wave propagation and focusing in inhomogeneous media," Shock Waves in Condensed Matter and Heterogeneous Media, Springer, pp. 439–444.

[13] Williams, J. C., Woodward, J. F., Stonechill, M. A., Evan, A. P., and McAteer, J. A., 1999, "Cell damage by lithotripter shock waves at high pressure to preclude cavitation," Ultrasound Med. Biol., **25**(9), pp. 1445–1449.

[14] Swanson, S. R., 1985, "A constitutive model for high elongation elastic materials," Trans. Am. Soc. Mech. Eng., **107**, pp. 110–114.

[15] Maksym, G. N., and Bates, J. H. T., 1997, "A distributed nonlinear model of lung tissue elasticity," J. Appl. Physiol., **82**, pp. 32–41.

[16] Saraf, H., Ramesh, K. T., Lennon, A. M., Merkle, A. C., and Roberts, J. C., 2007, "Mechanical properties of soft human tissues under dynamic loading," J. Biomech., **40**, pp. 1960–1967.

[17] Rosen, J., Brown, J. D., De, S., Sinanan, M., and Hannaford, B., 2008, "Biomechanical properties of abdominal organs in vivo and postmortem under compression loads," J. Biomech. Eng., **130**, pp. 021020–1 – 021020–17.

[18] Umale, S., Deck, C., Bourdet, N., Dhumane, P., Soler, L., Marescaux, J., and Willinger, R., 2013, "Experimental mechanical characterization of abdominal organs: liver, kidney & spleen," J. Mech. Behav. Biomed. Mater., **17**, pp. 22–33.

[19] Kemper, A. R., Santago, A. C., Stitzel, J. D., Sparks, J. L., and Duma, S. M., 2012, "Biomechanical response of human spleen in tensile loading," J. Biomech., **45**, pp. 348–355.
[20] Takaza, M., Moerman, K. M., and Simms, C. K., 2013, "Passive skeletal muscle response to impact loading: Experimental testing and inverse modelling," J. Mech. Behav. Biomed. Mater., **27**, pp. 214–225.
[21] Zhang, L., Yang, K. H., and King, A. I., 2001, "Comparison of brain responses between frontal and lateral impacts by finite element modeling," J. Neurotrauma, **18**(1), pp. 21–30.
[22] Carter, D. R., 1984, Biomechanics of bone, Appleton & Lange.
[23] Friedlander, F. G., 1947, "Simple progressive solutions of the wave equation," Math. Proc. Camb. Philos. Soc., **43**(3), pp. 360–373.
[24] Taylor, P. A., 1995, CTH Reference Manual: The Transverse Isotropic (TI) Model, Sandia National Laboratories.
[25] Gruss, E., 2006, "A correction for primary blast injury criteria," J. Trauma-Inj. Infect. Crit. Care, **60**(6), pp. 1284–1289.

DISTRIBUTION

1 US Navy Health Research Center
Attn: James Mackiewicz (electronic copy)
james.f.mackiewicz.civ@mail.mil

1 San Antonio Military Medical Center
Attn: Maj. Adam M. Willis, MD PhD (electronic copy)
adam.m.willis.mil@mail.mil

1 Office of Naval Research
Attn: Dr. Timothy B. Bentley (electronic copy)
Timothy.b.bentley@navy.mil

1 UNM Health Sciences Center
Attn: Dr. Corey C. Ford, MD PhD (electronic copy)
cford@salud.unm.edu

1 University of Texas at Austin
Attn: Dr. John T. Foster (electronic copy)
jfoster@austin.utexas.edu

1	MS0783	J. E. Pacheco	6626
1	MS0845	S. T. Miller	1542
1	MS0957	R. G. Spulak	5331
1	MS1153	D. R. Gardner	5444
1	MS1156	W. H. Rutledge	5430
10	MS1160	D. A. Dederman	5431
1	MS1160	D. J. Burnett	5431
15	MS1160	C. F. Cooper	5431
15	MS1160	P. A. Taylor	5431
1	MS1160	R. J. Terpsma	5431
1	MS1161	T. K. Stalker	5447
1	MS1164	D. W. Plummer	5400
1	MS1188	A. Nanco	6114
1	MS1231	J. S. Peery	5000
1	MS0899	Technical Library	9536 (electronic copy)
1	MS0359	D. Chavez, LDRD Office	1911
1	MS0161	Legal Technology Transfer Center	11500


Sandia National Laboratories